HHS Public Access

Author manuscript

Cell Stem Cell. Author manuscript; available in PMC 2023 June 08.

Published in final edited form as:

Cell Stem Cell. 2022 September 01; 29(9): 1315–1332.e9. doi:10.1016/j.stem.2022.07.010.

The mitochondrial protein OPA1 regulates the quiescent state of adult muscle stem cells

Nicole Baker[1], **Steven Wade**[1,6], **Matthew Triolo**[1,6], **John Girgis**[1], **Damian Chwastek**[1], **Sarah Larrigan**[1], **Peter Feige**[2], **Ryo Fujita**[3,4], **Colin Crist**[3], **Michael Rudnicki**[2], **Yan Burelle**[5], **Mireille Khacho**[1,7,*]

[1]Department of Biochemistry, Microbiology and Immunology, Center for Neuromuscular Disease (CNMD), Ottawa Institute of Systems Biology (OISB), Faculty of Medicine, University of Ottawa, Ottawa, ON, K1H 8M5, Canada

[2]Sprott Center for Stem Cell Research, Ottawa Hospital Research Institute, Regenerative Medicine Program, Department of Cellular and Molecular Medicine, Faculty of Medicine, University of Ottawa, Ottawa, ON, K1H 8L6, Canada

[3]Lady Davis Institute for Medical Research, Jewish General Hospital, Department of Human Genetics, McGill University, Montreal, Quebec, H3T 1E2, Canada

[4]Division of Regenerative Medicine, Transborder Medical Research Center, Faculty of Medicine, University of Tsukuba, Ibaraki 305-8575, Japan.

[5]Interdisciplinary School of Health Sciences, University of Ottawa, Ottawa, ON, K1H 8M5, Canada

[6]These authors contributed equally

[7]Lead contact

Summary

Quiescence regulation is essential for adult stem cell maintenance and sustained regeneration. Our studies uncovered that physiological changes in mitochondrial shape regulate the quiescent state of adult muscle stem cells (MuSCs). We show that MuSC mitochondria rapidly fragment upon an activation stimulus, via systemic HGF/mTOR, to drive the exit from deep quiescence. Deletion of the mitochondrial fusion protein OPA1 and mitochondrial fragmentation transitions

*Correspondence: mkhacho@uottawa.ca.

Author Contributions

MK conceptualized and led the study,
MK and NB designed and performed the majority of experiments,
MK and NB wrote the paper,
SW performed *in vivo* and *in vitro* OPA1-OE experiments, *in vitro* suspension and myofiber experiments, qPCR,
MT performed Seahorse analysis, some ATP assays, *in vivo* mitoTEMPO experiments, atrophy and myokine experiments,
JG provided technical support in initializing the study,
SL performed C2C12 qPCR with Rotenone and GSH treatment,
DC performed initial H&E counts following muscle injury,
PF, CC and RY provided guidance and technical training for MuSCs,
YB provided technical support,
MR provided guidance and animal models

Declaration of Interests

The authors declare no competing interests.

MuSCs into G-alert quiescence causing premature activation and depletion upon a stimulus. OPA1 loss activates a glutathione (GSH)-redox signaling pathway promoting cell-cycle progression, myogenic gene expression and commitment. MuSCs with chronic OPA1 loss, leading to mitochondrial dysfunction, continue to reside in G-alert but acquire severe cell cycle defects. Additionally, we provide evidence that OPA1 decline and impaired mitochondrial dynamics contribute to age-related MuSC dysfunction. These findings reveal a fundamental role for OPA1 and mitochondrial dynamics in establishing the quiescent state and activation potential of adult stem cells.

Introduction

Resident adult stem cells are essential for tissue homeostasis. Consequently, loss or dysfunction of adult stem cells is a unifying feature of many degenerative conditions and aging across many cell types (Almada and Wagers, 2016; Feige et al., 2018; Oh et al., 2014; Signer and Morrison, 2013). A unique and essential feature of adult stem cells is their existence in a reversible quiescent state (Blanpain et al., 2004; van Velthoven and Rando, 2019). Quiescence is fundamental to the preservation and longevity of stem cells (Cho et al., 2019; Tümpel and Rudolph, 2019; van Velthoven and Rando, 2019). As such, stem cell populations, including skeletal muscle stem cells (MuSCs), reside in a quiescent state until prompted by a stimulus to become activated, re-enter the cell cycle and mediate regeneration of adult tissue (van Velthoven and Rando, 2019). Moreover, the balance by which adult stem cells can reside in a quiescent state while retaining the ability to rapidly respond to activation cues is critical for long-term maintenance and an efficient regenerative potential (van Velthoven and Rando, 2019). Stem cell activation is mediated by well-established extrinsic and intrinsic molecular mechanisms that involve the stem cell niche, growth factors and key signaling pathways (Cheung and Rando, 2013; Cho et al., 2019; Dumont et al., 2015). How these mechanisms are coordinated and a potential central hub mediating this crosstalk are not fully understood.

An emerging characteristic defining the progressive stages of stem cell quiescence, activation or commitment is their metabolic and mitochondrial states (Chandel et al., 2016; Maryanovich et al., 2015; Ryall et al., 2015; Yucel et al., 2019). Excessive mitochondrial fragmentation and decreased expression of the mitochondrial fusion protein OPA1 is observed in aged or pathological conditions (Amartuvshin et al., 2020; Sebastián et al., 2017; Song et al., 2017; Tezze et al., 2017), which often encompass compromised stem cell quiescence and maintenance. Here we uncovered that OPA1 and mitochondrial dynamics regulate the quiescent state of adult MuSCs. Our study reveals that mitochondria undergo physiological and transient fragmentation, in response to an extrinsic activation stimulus, and transmit information intracellularly to establish the depth of quiescence and activation potential of MuSCs. Meanwhile, OPA1 deletion and unbalanced mitochondrial fragmentation, similar to pathological conditions and aging, places MuSCs in a G-alert state, with hypersensitive activation, rapid cell cycle re-entry and loss of stem cell maintenance.

Results

Loss of OPA1 impairs muscle stem cell maintenance following injury

Mitochondrial morphology was examined in MuSCs using an *in vitro* model of single EDL myofiber cultures at defined time points post-dissection representing the stages of activation ($Pax7^+$ cells between 0 and 24hrs), commitment ($MyoD^+$ cells at T=48hrs), and differentiation ($MyoD^+$ and MyoG+ cells at T=72 and 96hrs, respectively) (Brun et al., 2018; Pasut et al., 2013). Mitochondria in MuSCs undergo pronounced and transient changes in structure at different phases (Figure 1A). A striking increase in mitochondrial fragmentation, assessed by mitochondrial length and volume, was observed during the activation and commitment stages (Figure 1A-C), followed by mitochondrial elongation and increased mitochondrial mass during differentiation (Figure 1A-C and Figure S1A). This suggested that mitochondrial structural plasticity may play a role in MuSC function.

To understand the role of fragmentation in adult MuSCs, we generated an adult MuSC specific knockout of the essential mitochondrial fusion gene *OPA1* (*OPA1-Pax7CreERT2*, referred to as OPA1-MKO) (Figure 1D,E and Figure S1B, see STAR methods). Short-term loss (3 days following last TAM administration) of OPA1 in MuSCs did not reveal any detectable effect on global ATP levels (Figure S1C). Yet, OPA1 loss caused mitochondrial fragmentation in Pax7+ MuSCs (Figure 1F,G) and impaired the dynamic changes in mitochondrial shape, such that OPA1-MKO mitochondria were maintained in a fragmented state (Figure 1H). Upon initial examination, no detectable muscle phenotype was observed 3 days after OPA1 deletion. The size and number of existing myofibers, and the number of Pax7+ MuSCs were similar to the wild-type littermate controls (Figure 1I-K and Figure S1D-F). To observe whether OPA1 loss impacts MuSC function, a cardiotoxin (CTX) injury into the Tibialis Anterior (TA) muscle was performed 3 days after the last TAM administration and harvested at 21 days post-injury (DPI) (see paradigm in Figure S1G). OPA1-MKO exhibited a striking defect in muscle regeneration (Figure 1I and Figure S1H,I). Importantly, there was a severe depletion of the Pax7+ MuSC pool (Figure 1J,L and Figure S1J), indicating an impairment in self-renewal. These data show for the first time that OPA1 and potentially mitochondrial dynamics are essential for MuSC maintenance and function.

In the absence of OPA1 muscle stem cells are primed for activation and commitment

Short-term OPA1 loss revealed a decline in Pax7+ cells in OPA1-MKO TA muscle that began early in the regeneration process (4DPI) (Figure 2A-C and Figure S2A). The decline in Pax7+ cells in OPA1-MKO was not due to a general failure in MuSC activation and cell-cycle re-entry (EdU+ cells) or proliferation (Ki67+ cells) (Figure 2D-F). OPA1 loss did not induce muscle atrophy genes (*Atrogin1, Murf1*) or circulating mitokines (GDF15, FGF21), shown to cause MuSC depletion (Figure S2B,C) (Tezze et al., 2017). There was no indication of energy deficits in OPA1-MKO MuSCs under basal (uninjured) conditions or following injury (7DPI), as global and oligomycin-sensitive ATP (mitochondrial-generated ATP) levels were comparable to controls (Figure 2G). Metabolic analysis did not reveal any detectable difference in overall mitochondrial respiration (OCR) or glycolytic metabolism (ECAR) in freshly isolated MuSCs (Figure 2H,I). In addition, short-term loss of OPA1 did not alter cristae width or number (Figure S2D-G) and did not induce cell death or

Cytochrome C release (Figure S2P-R). However, we observed a concomitant increase in the number of committing and differentiating cells (MyoD+ and MyoG+ cells) at 4DPI (Figure 2J,K and Figure S2H-K) that was not due to any significant increase in proliferation (Figure S2L,M). This suggested that OPA1 deletion drives MuSC commitment, in line with previous studies showing that mitochondrial fragmentation promotes stem cell commitment (Buck et al., 2016; Civenni et al., 2019; Forni et al., 2016; Khacho et al., 2016; Zhong et al., 2019). Thus, myofibers were cultured over a period of 72hrs to observe MuSC characteristics and fate decisions *in vitro*. First, there was no difference in the number of Pax7+ MuSCs on freshly isolated myofibers (T=0hrs) from OPA1-MKO or after 24hrs in culture (Figure S2N,O), and no differences in cluster size (Figure S2S). Following 72hrs, OPA1-MKO MuSCs had a greater propensity to commit to a myoblast fate (MyoD+ and MyoG+ cells) at the expense of self-renewal (Pax7+ cells) (Figure 2L-N). Together these data validate that OPA1-MKO MuSCs have an increased capacity to commit and indicate an important role for OPA1 and mitochondrial dynamics in MuSC maintenance and fate decisions.

During tissue analysis from the CTX injury experiments, we unexpectedly discovered that OPA1-MKO animals also exhibit a decline in Pax7+ cells in the uninjured contralateral limb (Figure 2O), which was accompanied by a small increase in MyoD+ cells (Figure 2P). The increased propensity of distal OPA1-MKO MuSCs commit was also observed in myofibers isolated from the contralateral limb at 21DPI following a CTX injury (Figure 2Q,R). Thus, OPA1 loss may hypersensitize MuSCs to an activation stimulus causing distal MuSCs to undergo premature activation and cell cycle re-entry. Furthermore, Pax7+ MuSCs on the contralateral limb had increased EdU incorporation and Ki67 expression in OPA1-MKO (Figure 2S,T). We also detected MyoD+ cells that incorporated EdU or expressed Ki67 in the contralateral limb (Figure 2U) indicating that distal MuSCs were highly responsive in OPA1-MKOs, resulting in premature activation. The resemblance of this phenotype to the G-alert quiescent state, which lies between a deep quiescence (G0) and an activated state (G1) identified by Rogers et al. (Rodgers et al., 2014), led us to question whether OPA1 is a regulator of stem cell quiescence.

Mitochondria undergo transient morphological changes during the transition from quiescence to activation in MuSCs

We sought to understand the kinetics and initial timing of mitochondrial fragmentation in a wild-type setting. Using the *in vitro* single EDL myofiber culture model, mitochondrial fragmentation was detectable at the onset of MuSC activation (4hrs in culture) (Figure S3A) and remained fragmented at 12-24hrs (Figure 3A-C and Figure S3B). Importantly, the timing of mitochondrial fragmentation far precedes proliferation or Ki67 expression, which is only detected at 24hrs (Figure S3C)(Miller et al., 2018). Next, we asked if mitochondrial fragmentation occurs during MuSC activation *in vivo*. Myofibers isolated from the contralateral limb following a CTX injury showed evident mitochondrial fragmentation in MuSCs at the onset of MuSC activation *in vivo* (2DPI), prior to major proliferation at 4DPI (Figure 3D) (Murphy et al., 2011). In addition, freshly isolated MuSCs at 2DPI showed a significant decrease in *OPA1* expression (Figure 3E). Decreased OPA1 protein expression was also observed in activated MuSCs *in vitro* (Figure S3D). These data are consistent with

a potential physiological role for decreased OPA1 and changes in mitochondrial dynamics during MuSC exit from quiescence and switch towards the activated state.

Of note, mitochondria resume an elongated morphology beginning at 48hrs (Figure 3B,C) and more prominently by 72 and 96hrs (Figure 1A-C and Figure S1A). In general, by 48hrs Pax7+ cells have divided and the resulting daughter cells represent a heterogenous population of self-renewing MuSCs (Pax7-high cells) and committed myoblasts (Pax7-low cells) (Rocheteau et al., 2012). Therefore, quantification of mitochondrial length based on Pax7 expression level showed that mitochondrial elongation is re-instigated in the Pax7-high cells (Figure S3E,F), suggesting that MuSCs resuming a quiescent state (ie. self-renew) may re-establish the initial elongated mitochondrial morphology observed at T=0hrs.

Disruption of OPA1 and mitochondrial dynamics alters the quiescent state of MuSCs

Data thus far present a potentially unique role for OPA1 and mitochondrial dynamics in the regulation of stem cell quiescence and activation. We reasoned that OPA1-MKO MuSCs, which exhibit mitochondrial fragmentation in intact muscle (Figure S3G), may already exist in a G-alert quiescent state *in vivo* and would rapidly enter the cell cycle upon a stimulus. As expected, there was increased EdU incorporation and Ki67 co-labelling with Pax7+ cells at 2DPI in the injured limb of OPA1-MKO mice (Figure 3F), prior to generalized MuSC proliferation at 4DPI. OPA1-MKO myofibers, isolated from the contralateral limb, also had increased Pax7/Ki67+ cells already at time of fixation (T=0hrs), with a cell cycle entry kinetics that exceeded that of OPA1-WT (Figure 3G). Similarly, OPA1-MKO myofibers not subjected to any injury (intact) had increased Pax7/Ki67+ cells over time compared to OPA1-WT (Figure 3G). In addition, OPA1-MKO MuSCs had a larger cell diameter and higher propensity to express pS6 protein (Figure 3H,I and Figure S3H,I), consistent with hallmarks of G-alert quiescence (Rodgers et al., 2014; van Velthoven and Rando, 2019). The nuclear morphology of Pax7+ MuSCs from OPA1-MKO myofibers isolated from both intact (uninjured) or contralateral limbs following an injury had a higher proportion with a rounded nuclear morphology of activated cells and a smaller proportion with planar elongated nuclei consistent with more quiescent cells (Eliazer et al., 2019) (Figure 3J and Figure S3J). By 24hrs the majority of OPA1-WT MuSCs had reached the activated state, while OPA1-MKO MuSC had surpassed this phase, reaching a late activation or early committed state represented by larger nuclei (Figure S3J) (Heo et al., 2016). These data demonstrate that in the absence of OPA1, MuSCs exist in a G-alert quiescent state and can more readily undergo activation and cell cycle re-entry upon a stimulus.

Consistent with these data, freshly isolated MuSCs from intact OPA1-MKO muscle showed a significant decrease in quiescence and self-renewal genes, including *Pax7*, *CD34*, and *Hes1* (Figure 3K and Figure S3K,L). To get a global outlook, RNAseq analysis was performed on freshly FACS sorted MuSCs from OPA1-MKO and OPA1-WT muscle 3 days following last TAM administration. This revealed about 70 differentially regulated genes (with a log2FC of ≥1.0 or ≤−1.0; padj values ≤0.05) (Figure 3L,M), with gene ontology (GO) terms relating to cell cycle, proliferation, chromosome changes and myogenesis (Figure 3N,O). These genes included cell cycle regulators (*Cdk1*, *Rgcc*), myogenesis regulators (*MyoG*, *Mymk*) and genes that promote proliferation, chromosome changes and

spindle morphology (*Ncaph*, *Spc25*) (Figure 3P and Figure S3M). The seemingly direct effects on such gene classes provides some mechanistic insight into the ability of OPA1 loss to rapidly alter the state of MuSCs.

Next, we investigated the role of mitochondrial dynamics in regulating the quiescent state of MuSCs by pharmacological manipulation using a low dose (2μM) of the DRP1-mediated mitochondrial fission inhibitor Mdivi-1 (see Figure S3N and Figure S5M). Treatment of wild-type myofibers with Mdivi-1 prevented the natural course of mitochondrial fragmentation observed in MuSCs at 4hrs (Figure 3Q). Consequently, Mdivi-1 treatment caused a significant delay in Ki67 expression and overall less Pax7/Ki67+ cells (Figure 3R). Furthermore, MuSCs treated with Mdivi-1 retained a planar elongated nuclear morphology (Figure 3S) in line with a more quiescent state (Eliazer et al., 2019). Mdivi-1 also altered MuSC cell fate with a shift towards self-renewal (Pax7+ cells) (Figure 3T). Importantly, Mdivi-1 restored the activation kinetics of OPA1-MKO MuSCs to wild-type levels (Figure 3U) and reestablished the balance of fate decisions towards self-renewal (Pax7+/MyoD− cells) (Figure 3U). These results provide evidence that manipulation of mitochondrial structure can regulate the quiescent state of MuSCs and demonstrate an important role for mitochondrial dynamics in MuSC maintenance.

Mitochondrial shape changes occur in response to external stimuli to regulate the quiescent state of MuSCs

We hypothesized that systemic signaling may be an upstream mechanism to promote physiological mitochondrial fragmentation in MuSCs. Release of the systemic hepatocyte growth factor activator (HGFA) upon injury and cleavage to its active form HGF (aHGF) activates mTORC1 to induce G-alert in MuSCs (Rodgers et al., 2017). Consistent with previous reports, treatment with exogenous aHGF or HGFA promoted Ki67 expression (cell cycle entry) in Pax7+ cells, while mTOR inhibition with Rapamycin had the opposite effect (Figure 4A). Next, exogenous aHGF or HGFA caused a modest but further increase in mitochondrial fragmentation starting at 4hrs (Figure 4B-D and Figure S4A-D). EDL myofiber media already contains HGF that could mask the effects of additional exogenous aHGF or HGFA, thus myofibers were cultured without any HGF for a short period (4hrs). As expected, there was no detectable signs of mitochondrial fragmentation in the absence of HGF in the media (Figure 4E-G). Meanwhile, a decreased dose of HGF (25% HGF) led to partial mitochondrial fragmentation (Figure 4E,F). Importantly, reintroduction of exogenous aHGF to the media completely restored mitochondrial fragmentation (Figure 4E-G). However, addition of exogenous aHGF in the presence of Mdivi-1 prevented these changes (Figure 4N,O). Furthermore, *in vivo* administration of recombinant HGFA, which activated the mTOR pathway (increased Pax7/pS6+ cells) and enhanced MuSC activation (Figure 4H,I,J and Figure S4E), showed a striking level of mitochondrial fragmentation in MuSCs (Figure 4K,L and Figure S4F). Next, inhibition of mTOR with Rapamycin or Torin-1 prevented mitochondrial fragmentation in culture, to the same degree as Mdivi-1 (Figure 4B,C,M and Figure S4A-D). Furthermore, addition of exogenous aHGF together with Rapamycin also prevented mitochondrial fragmentation in MuSCs (Figure 4N,O). These data validate the requirement for mTOR and demonstrate the ability of mitochondria

to sense external stimuli and relay the HGF/mTOR-mediated signal for the exit of MuSCs from a quiescent state.

Mitochondrial fragmentation mediates myogenic commitment of MuSCs through changes in glutathione/redox states

Thus far we present a multi-faceted and stage-dependent function for mitochondrial fragmentation, in regulating MuSC quiescence/activation (Figure 3) and promoting commitment (Figure 2). To unravel downstream signaling mechanisms, metabolic and redox assessments were performed. Short-term loss of OPA1 in MuSCs did not reveal any detectable energy deficits (Figure S1C and Figure 2G,H). There was no detectable differences in the metabolic shift following transition from quiescence to activation (Ryall et al., 2015), as measured by ATP levels, OCR and ECAR at 24hrs in culture (Figure S5A-C). Next, we examined mitochondrial ROS (mtROS) given the importance of redox signaling in other stem cell systems (Khacho et al., 2016; Paul et al., 2014; Tormos et al., 2011). Analysis with MitoSOX showed a small but significant increase in mtROS in OPA1-MKO MuSCs (Figure 5A and Figure S5D,E,F). In addition, OPA1-MKO MuSCs had decreased gene expression of mtROS regulators *SOD2* and *UCP2*, and increased levels of the redox marker *SLC7a11* (*Xct*) (Figure 5B).

Increased expression of *SLC7a11*, a direct target of the NRF2 redox response pathway for glutathione (GSH) biosynthesis (Shin et al., 2017), and a recent link between OPA1 and GSH (Patten et al., 2021) prompted further investigation. Expression of glutathione synthetase (*GSS*) and glutamate cysteine ligase (*GLCL*) were upregulated in freshly isolated MuSCs from OPA1-MKO (Figure 5B). Interestingly, similar changes were detected comparing wild-type MuSCs to myoblasts (Figure 5C,D and Figure S5G). Thus, mitochondrial fragmentation may mediate changes in MuSC properties by a GSH/redox mechanism. Given the scarcity of the MuSC population it was not possible to examine GSH levels using HPLC. Yet, preliminary metabolomics analysis showed higher GSH levels in myoblasts compared to MuSCs (Figure S5H). Thus, using an antibody approach to detect the GSH status in MuSCs, we observed that wild-type MuSCs accumulate staining following activation (24hrs in culture) (Figure 5E). Importantly, OPA1-MKO MuSC already exhibit higher GSH status upon isolation (T=0hrs) that remain high during the activation process (Figure 5E and Figure S5L).

We questioned whether GSH, in this context, may relay mitochondrial- and mtROS-mediated effects in MuSCs. Treatment of cultured myoblasts with low dose Rotenone (10 nM), to mimic a small increase in mtROS levels (Figure S5O) (Murphy, 2009), led to increased intracellular levels of reduced and oxidized GSH/GSSG measured by HPLC (Figure S5I) and elevated expression of all components of the GSH biosynthesis pathway (Figure S5J). Increased mtROS (Figure S5O,P) also increased GSH staining in MuSCs (Figure S5K). This led us to hypothesize that increased mtROS and GSH redox status may be responsible, in part, for the OPA1-MKO MuSCs phenotype. Indeed, treatment of myofibers in culture with the mtROS antioxidant mitoTEMPO (Hu and Li, 2016) or the inhibitor of GSH synthesis BSO (Tagde et al., 2014) (Figure S5L,M) reversed the cell cycle entry kinetics of OPA1-MKO MuSCs (Figure 5F). mitoTEMPO also reversed

the expression changes of cell cycle genes altered in OPA1-MKO MuSCs (Figure 5G). Furthermore, reducing mtROS or GSH restored the self-renewal capacity of OPA1-MKO MuSCs (Figure 5H). In addition, *in vivo* treatment of OPA1-MKO mice with mitoTEMPO (Figure S5N) partially restored the kinetics of cell cycle re-entry and the G-alert phenotype of OPA1-MKO MuSCs to wild-type levels (Figure 5I-K).

To test if mtROS/GSH states can impact wild-type MuSC activation and/or commitment, myofibers were cultured with compounds that alter mtROS and GSH levels. Low dose Rotenone or mito-Paraquat, and exogenous GSH or cysteine significantly enhanced MuSC cell cycle entry (Figure 5L and Figure S5Q) and commitment (Figure 5M and Figure S5R,S). In contrast, dampening mtROS levels (mitoTEMPO) or intracellular GSH (BSO) resulted in delayed Ki67 expression (Figure 5L), enhanced self-renewal (Figure 5M) and a nuclear morphology consistent with a more quiescent state (Figure S5S). Furthermore, Rotenone and GSH decreased *Pax7* and *CD34* gene expression (Figure 5N,P), while increasing *MyoD* and *MyoG* (Figure 5 O,P). In addition, Rotenone treatment increased expression of cell cycle regulatory genes identified by RNAseq to be upregulated in OPA1-MKO MuSCs (Figure 5O). Meanwhile, treatment of cells with Rotenone in the presence of BSO prevented the increased expression of *MyoD* and *MyoG* (Figure 5Q and Figure S5T). Importantly, Mdivi-1 suppressed the expression of *MyoD* and *MyoG*, suggesting that mitochondrial fragmentation may be the upstream controlling mechanism (Figure 5Q). Together these data indicate that changes in GSH, which is elevated by OPA1 loss and increased mtROS, may serve as a downstream signal to promote MuSC activation/commitment.

Chronic loss of OPA1 and persistent mitochondrial fragmentation leads to severe MuSC defects

Next, we asked whether prolonged OPA1 loss and chronic mitochondrial fragmentation could further impact MuSC function. We developed a chronic model of OPA1 loss (1- and 3-month OPA1-MKO, see STAR methods). MuSCs with sustained loss of OPA1 and mitochondrial fragmentation (Figure S6A,B) showed detectable signs ATP decline and impaired mitochondrial respiration (OCR) (Figure 6A,B and Figure S6C,D). Thus, within this chronic model, as opposed to the acute OPA1-MKO model, MuSCs exhibit signs of mitochondrial dysfunction.

Examination of 3-month OPA1-MKO animals under basal conditions showed no detectable difference in myofiber size and numbers (Figure S6E,F) or number of Pax7+ MuSCs (Figure 6C,D). However, MuSCs examination following injury or upon isolation revealed an extensive level of dysfunction, that was more pronounced and occurred earlier than in the acute OPA1-MKO model. At 7DPI following CTX injury in one limb, 3-month OPA1-MKO animals had impaired muscle regeneration (Figure S6E,G), an almost complete loss of Pax7+ MuSCs in the injured limb (Figure 6C,E) and MuSC depletion in the contralateral limb (Figure 6C,F). Freshly isolated myofibers (T=0hrs) from 1- and 3-month OPA1-MKO mice had significantly higher Pax7+ cells expressing the G-alert marker pS6 (Figure 6G and Figure S6H), a nuclear morphology consistent with activated MuSCs (Figure S6I,J) and enhanced activation kinetics as assessed by MyoD expression (Figure 6H and S6K). Freshly

isolated MuSCs showed decreased expression of Pax7 and *CD34* in 3-month OPA1-MKO (Figure 6I), similar to acute OPA1 loss (Figure 3K). These data provide evidence that MuSCs reside in a G-alert state when OPA1 is deleted both acutely and chronically.

Despite enhanced activation (Figure 6H and S6K), individual MuSCs in 3-month OPA1-MKO did not appear to undergo cell division (Figure 6J,K). This was apparent at 1-month (Figure S6L) but became more severe with age, such that 3-month OPA1-MKO MuSCs had an average cluster size of one cell over 72hrs in culture (Figure 6J,K), and failed to express Ki67 (Figure 6L and Figure S6L). In addition, 3-month OPA1-MKO MuSCs could not pass the G1 cell cycle restriction point (R-point), as determined by expression of phosphorylated retinoblastoma protein (pRb) (Figure 6M). Regardless of the cell cycle defect, each individual MuSC from 3-month OPA1-MKO underwent activation/commitment, as all cells expressed MyoD (Figure 6K,N). The preferential commitment of MuSC was also observed in 1-month OPA1-MKO (Figure S6M), similar to the acute model. We reasoned that the additional proliferation defects by chronic OPA1 loss may be due to mitochondrial dysfunction (Figure 6A,B and Figure S6C,D). Indeed, impairing OXPHOS in MuSCs caused a significant decline in MuSC proliferative capacity (Figure S6N,O). Together, these data further solidify that OPA1 and mitochondrial fragmentation regulate MuSCs quiescent state and activation potential independent of mitochondrial OXPHOS function.

In contrast to acute OPA1 loss, MuSCs from 3-month OPA1-MKO exhibited decreased levels of *SLC7a11*, *GLCL* and *GSS* mRNA (Figure 6O), suggesting a potential depletion of the GSH pool. Interestingly, GSH depletion using high dose BSO (50 μM) also prevented MuSC proliferation in a wild-type setting (Figure S6N,O). Thus, we tested whether addition of GSH or cysteine/glycine (cys/gly), to increase GSH levels, could reverse any MuSC dysfunction in 3-month OPA1-MKO and found that this restored the expression of Ki67 and the number of MuSCs capable of passing the R-point (Figure 6P,Q). However, it did not promote MuSC cell division and increase cluster size (Figure 6R), suggesting additional GSH-independent cell cycle defects in 3-month OPA1-MKO MuSCs. Nonetheless, cell fate analysis showed that increasing GSH levels can potentially restore the number of Pax7+ cells in 3-month OPA1-MKO MuSCs (Figure 6S).

Decreased OPA1 and impaired mitochondrial dynamics are observed during physiological MuSC aging and impact MuSC function

Excessive mitochondrial fragmentation and redox imbalance are often implicated in the pathogenesis of degenerative diseases and aging. A decline in OPA1 has been observed in aging muscle and contributes to skeletal muscle degeneration (Tezze et al., 2017). However, mitochondrial dynamics and OPA1 have not been examined in aged MuSCs. Using available gene micro-array data (Liu et al., 2013) comparing MuSCs from young (2 month) and old (24 month) mice, we found decreased *OPA1* expression during aging (Figure 7A). Furthermore, selecting genes based on gene ontology (GO) terms related to mitochondrial dynamics and function, and redox regulation revealed that aged MuSCs exhibit changes in genes involved in mitochondrial organization and OPA1 processing (Pari, Phb) (Anderson et al., 2020; Ishihara et al., 2006), oxidative phosphorylation (OXPHOS Complex-1, -III and

-V subunits), redox and glutathione homeostasis (Figure 7A and Figure S7A). Alterations in *OPA1* and other mitochondrial dynamics genes were also found in aged MuSCs during injury-induced activation in a dataset from Shchedrin *et al.* (Shcherbina et al., 2020)(Figure S7B,C). We compared micro-array data by Alonso-Martin *et al.* (Alonso-Martin et al., 2016) using 2 and 18 month (aged) MuSCs, to determine if changes are present earlier in the aging process. This showed 1042 common genes significantly altered in the Liu *et al.* and Alonso-Martin *et al.* datasets (based on Log2FC >1.0 and <−1.0, and padj values <0.05) (Figure S7D), with 111 (10.9%) being related to mitochondria and 40 (3.9%) genes implicated in redox homeostasis (Figure S7E). Thus, *OPA1*, mitochondrial dynamics and GSH/redox may be implicated in age-associated MuSC impairment.

Since the aging process may begin during middle-age (Del Campo et al., 2018; Price et al., 2014; Sayed et al., 2016), a three-way comparative analysis was performed between altered genes at 18 and 24 months (from Liu *et al.* and Alonso-Martin *et al.*) with data from Sinha *et al.* (Sinha et al., 2014) comparing 2- and 12-month MuSCs. This did not reveal many common significantly changed genes in 12-month MuSCs (Figure S7F), but a curated search showed similar trends in gene expression changes to those at 18 and 24 months (padj >0.05) (Figure 7B). For example, the Log2FC of *OPA1* revealed a potential early onset down-regulation (Figure 7B). Similar trends are observed for mitochondrial dynamics genes (*DRP1*, *MFF*), OPA1 related genes (*Yme1l1*, *Parl*, *Phbs*) and GSH/redox related genes (*SOD2*, *NRF2*, *SLC7a11*, *Glcl*) (Figure 7B). To gain a global perspective of this trend, the 24-month curated gene list (Figure 7A and Figure S7A) was compared with the 12- and 18-month datasets (Figure 7C and Figure S7G). All selected genes showed similar or trending Log2FC values with increasing significance (padj values) upon approaching old age (Figure 7C and Figure S7G). Together, these data suggest that expression changes for genes related to mitochondrial dynamics, function and redox homeostasis may begin as early as middle-age.

To test if mitochondrial dynamics are disrupted early during MuSC aging, we used 12-16 month mice (intermediate aging) that already show decreased *Pax7* gene expression (Figure 7D) and modest yet significant MuSC (Pax7+) depletion basally and 7DPI following a CTX injury (Figure 7E) (Blau et al., 2015; Price et al., 2014). *OPA1* expression was significantly declined in MuSCs at this age (Figure 7D), with variable changes in other mitochondrial dynamics genes (Figure 7D). There was also increased mitochondrial fragmentation in aging MuSCs (Figure 7F-H). Furthermore, MuSCs from aging mice showed increased commitment at the expense of self-renewal (Figure 7I) without any difference in cluster size (Figure 7J), and a nuclear morphology consistent with a more activated state (Figure 7K), similar to OPA1-MKO. Importantly, Mdivi-1 prevented mitochondrial fragmentation (Figure 7L) and restored MuSC fate (Figure 7M). Lastly, we asked whether increased levels of OPA1 can preserve MuSCs during aging. Transgenic OPA1-OE mice, with enhanced *OPA1* expression (Figure 7N and STAR methods) and elongated mitochondria (Figure 7O) in MuSCs, were aged for 12 months and subjected to a triple CTX injury, to test MuSC maintenance capacity (Figure S7H). OPA1-OE mice had significantly higher Pax7+ cells (Figure 7P). Since MuSC preservation in OPA1-OE may be due to the whole-body over-expression of OPA1, *in vitro* experiments were performed. MuSCs from 12-14 months OPA1-OE had slower kinetics of cell cycle re-entry (Figure 7Q,R), suggesting that OPA1-

OE potentially reside in a deeper quiescent state. In addition, OPA1-OE exhibited a greater proportion of Pax7+ MuSCs, suggesting an enhanced self-renewal capacity (Figure 7S). These data provide evidence that OPA1 and mitochondrial dynamics may play an important role in MuSC maintenance during aging.

Discussion

Our study reveals that OPA1 and mitochondrial structural plasticity serve as a physiological rheostat that controls the depth of quiescence and activation potential of MuSCs. This puts forth a view of mitochondria as regulators of stem cell quiescence and internal sensors of environmental stimuli that transmit stem cell activation signals. These findings provide important insights into the contribution of mitochondrial disruptions to adult stem cell dysfunctions in pathological conditions and aging, (see Figure S7I summary model)

Quiescence is a graded phase, whereby the promptness of stem cell activation is gauged by the depth of quiescence in which they exist (Rodgers et al., 2014; Rodgers et al., 2017; van Velthoven and Rando, 2019). The depth of quiescence of MuSCs is regulated by crosstalk between the microenvironment and cell intrinsic mechanisms (Rodgers et al., 2014; Rodgers et al., 2017). Our findings reveal that changes in mitochondrial structure serve to integrate and transmit the crosstalk between the environmental message and intrinsic cellular response mechanism. Intriguingly, the extent of mitochondrial fragmentation is determined by the strength of the systemic activation signal. This presents a scenario whereby a strong activation stimulus (or high systemic factor) at the injury site would generate a more fragmented phenotype required to drive stem cells out of quiescence. Meanwhile, stem cells at a distal location receive enough stimulus to induce only moderate fragmentation rendering a G-alert state that serves as a priming implement. We propose that elevated levels of systemic factors, observed during aging or diseases (Brack et al., 2007; Carlson et al., 2008; Chakkalakal et al., 2012; Gopinath and Rando, 2008), may contribute to aberrant mitochondrial fragmentation and altered MuSC quiescence. Altogether, this demonstrates a fundamental role for mitochondrial dynamics in modulating the graded G_0 to G-alert quiescent states of adult stem cells.

Our study uncovers that GSH is a downstream redox signaling molecule in adult MuSCs. While it is well established that ROS are potent signaling molecules that promote stem cell commitment (Ansó et al., 2017; Khacho et al., 2016; Lyublinskaya et al., 2015), this study shows the coordination of both mtROS and GSH in the modulation of MuSC activation, cell cycle progression and fate decisions, at least in part by eliciting changes in nuclear gene expression. To our knowledge, this represents a previously unappreciated and essential role for GSH as a signaling molecule, beyond its role in antioxidant defense, that significantly influences stem cell biology.

Our model of chronic OPA1 ablation and prolonged mitochondrial fragmentation in MuSCs embodies an accelerated aging model with the classical hallmarks of stem cell aging (Chakkalakal et al., 2012). This work also identifies defects in mitochondrial dynamics and redox homeostasis early in MuSC aging. Since any dysfunction to mitochondrial dynamics would lead to substantial impairments in many aspects of stem cell functions, excessive

fragmentation in pathological conditions or aging may represent an etiological factor in stem cell dysfunction. Thus, the ability to target mitochondrial dynamics before the onset of major stem cell dysfunction or senescence during aging and diseases presents a potential therapeutic strategy in regenerative medicine.

Limitations of the Study

Our work used genetic models of OPA1 loss or overexpression. Thus, the precise role for mitochondrial dynamics remains open. This was investigated using pharmacologically with Mdivi-1, but was limited to *in vitro* experiments. The role of mitochondrial dynamics in quiescence will be better delineated using genetic manipulation of other mitochondrial dynamics proteins (i.e., DRP1 or MFN1/2 knockouts). The difficulty in capturing MuSCs in deep quiescence restricted our ability to observe mitochondrial morphology and other characteristics in a native state. Future work will utilize an *in vivo* fixation method, that maintains mitochondrial integrity, to study organellar morphology and gene expression in quiescent MuSCs. Finally, the measure of GSH in MuSCs was a challenge given the scarcity of MuSCs and HPLC-mediated quantification requires a large cell number. Though we attempted to overcome this issue using an antibody approach, this renders a semi-quantitative assessment of GSH status and does not provide a redox state (GSH vs GSSG). The use of sensitive metabolomics techniques will provide more insight into the role of GHS in stem cell homeostasis.

STAR Methods

RESOURCE AVAILABITLY

Lead contact—Further information and requests for resources and reagents should be directed to and will be fulfilled by the lead contact, Mireille Khacho (mkhacho@uottawa.ca).

Materials availability—This study did not generate new unique reagents.

Data and code availability

- RNA-Seq data have been deposited in the NCBI Gene Expression Omnibus and are publicly available as of the date of publication. The accession number is listed in the key resources table. This paper analyzes existing, publicly available data. The accession numbers for the datasets are listed in the key resources table. All data reported in this paper will be shared by the lead contact upon request.
- This paper does not report original code.
- Any additional information required to reanalyze the data reported in this paper is available from the lead contact upon request.

EXPERIMENTAL MODEL AND SUBJECT DETAILS

Animals—Animal protocols were approved by the University of Ottawa's Animal Care Ethics Committee and adhered to the guidelines of the Canadian Council on Animal Care. All mice were housed and maintained at the Animal Care and Veterinary Service (ACVS)

of the University of Ottawa. OPA1$^{flox/flox}$ mice (Zhang et al., 2011) (kindly provided by Dr. Ruth Slack at the University of Ottawa) were crossed with Pax7CreERT2 mice (Murphy et al., 2011) to develop a Tamoxifen inducible and conditional knockout of OPA1 in Pax7+ adult MuSCs (*OPA1-Pax7CreERT2*, referred to as OPA1-MKO), providing an adult muscle stem cell specific knockout of OPA1. Mice that were OPA1-floxed and expressed the CreERT2 recombinase were used as OPA1 MuSC knockout (OPA1-MKO) mice, and littermate mice that were OPA1-floxed but did not possess the CreERT2 recombinase were used as wild-type controls (OPA1-WT). At 7-9 weeks of age, all mice received Tamoxifen (200 mg/kg) (Sigma T5648, 50 mg/mL dissolved in corn oil) administration via oral gavage for five consecutive days, followed by three days rest before any subsequent procedures were carried out. Specificity of *OPA1* deletion in MuSCs, and not muscle or other tissues, following Tamoxifen (TAM) administration (at 6-10 weeks of age) was validated by qPCR (Figure 1E and Figure S1B). A chronic model of OPA1 loss was developed by administering TAM at 8-10 weeks and allowing animals to age up to an additional 3 months (1-month and 3-month OPA1-MKO). See Figure S6A,B for validation of sustained OPA1 loss and mitochondrial fragmentation in 3-month OPA1 MKO. A mixture of both male and female mice were used for all experimental procedures. For experiments conducted with wild-type mice, C57Bl6J mice from the Pax7CreERT2 colony at age 7-10 weeks were used. For initial mitochondrial assessment in Figure 1A, 7-10 weeks old Pax7-GFP mice, kindly provided by Dr. Shahragim Tajbakhsh, were used (Sambasivan et al., 2009). For aging experiments 12-16 month old C57Bl/6J mice were used. For OPA1 over-expression experiments in Figure 7N-S, transgenic mice with a targeted whole-body mild (1.5x) OPA1 overexpression (OPA1-OE) were utilized (Varanita et al., 2015). OPA1-OE mice were rederived from mice originally described in Varanita et al. 2015 (Varanita et al., 2015) and provided as a kind gift from Dr. Ruth Slack.

Muscle stem cell isolation and culture

Magnetic Activated Cell Sorting (MACS): Muscle stem cells isolated using MACS isolation was carried out using an isolation kit purchased from Milteny Biotech (Porpiglia, E. & Blau, H.M. 2016). Following cervical dislocation, the Tibialis Anterior (TA), Extensor Digitorum Longus (EDL), gastrocnemius, soleus and quadriceps from the mouse hindlimb were harvested and minced. Next, 5 mL of digestion enzyme cocktail containing 1% (w/v) Collagenase B (Roche 11088831001) and 0.4% (w/v) Dispase II (Roche 04942078001) was added. Muscle tissue and enzyme mixture was placed in a C-Tube (Milteny Biotech130-093-237) and subjected to dissociation using the Milteny MACS Octo-Dissociator with customized programs (SLICE_FACS), previously published by Sincennes *et al.* (Sincennes et al., 2017), that perform rapid mechanical and enzymatic dissociation within 27 min. The muscle slurry was then run through a 100 μm filter (Fisher Scientific 22363549) and cells were spun down at 600xg for 10 min. The resulting pellet was treated with 400 μL of red blood cell lysis buffer (Sigma R7757) for 30 sec, followed by addition of 10 mL PBS and centrifugation at 600xg for 5 min. Muscle stem cells were subjected to negative selection using the Satellite Stem Cell Isolation Kit (Milteny 130-104-268), followed by an Anti-Alpha Integrin-7 muscle stem cell selection (Milteny 130-104-261) to obtain a relatively pure population of nearly quiescent muscle stem cells (cell population validation is shown in Figure S3G). See Figure S3K for validation of MuSC isolation

method. For culture conditions, MACS isolated MuSCs were cultured in a 24-well sterile plate, in 1mL of muscle stem cell culture media (FLAM's F-10 1X media supplemented with 20% FBS (v/v), 1% penicillin-streptomycin (v/v) and 2.5ng/ μL bFGF). Cells were treated with 10nM Rotenone, 24 mM GSH or 10 μM mitoTEMPO for 24 hours and harvested for further analysis.

Fluorescence Activated Cell Sorting (FACS): Mice aged 7-10 weeks were sacrificed by cervical dislocation and muscle tissue from the hindlimbs (see MACS section for list of hindlimb muscles) was harvested and digested in 1% (w/v) Collagenase-B (Roche 11088831001) and 0.4% (w/v) Dispase II (Roche 04942078001) using the Milteny MACS Octo-dissociator SLICE_FACS program for 27 minutes (as described in the MACS section above). Following digestion, the muscle slurry was filtered using a 100 μm filter (Fisher Scientific 22363549) and spun at 600g for 10 minutes to obtain a cell pellet, which was then subjected to red blood cell lysis using 400 μL of red blood cell lysis buffer (Sigma R7757) for 30 sec, followed by a wash with 10 mL of FACS buffer (3mM EDTA, 10% (v/v) FBS in 1x PBS) and subsequently spun at 600xg for 5 min. The cell pellet was then resuspended in 1 mL of FACS buffer. PE-conjugated antibodies were added, including the Lin-antibodies: Sca-1 (BD Pharmingen, 553108), CD45 (BD Pharmingen, 553081), CD31 (BD Pharmingen, 553373) and CD11b (eBiosciences, 12- 0112-82) to remove non-muscle stem cells present in the population. 647-conjugated α-integrin-7 (Ablab, 67- 0010-05) and PE-Cy7-conjugated VCAM (Biolegend, 105720) antibodies were used to positively select for muscle stem cells. Antibodies were incubated with the cell slurry for 15-25 min at 4°C, then topped up to 15mL with FACS buffer and spun at 600xg for 5 min. The pellet was resuspended in 2-3 mL of FACS buffer and filtered through a 40 μm Flowmi filter (Millipore Sigma BAH136800040) into a 5 mL polypropylene round-bottom tube (Falcon 352063). Samples were taken to the FACS sorter at the Flow Cytometry facility at the Ottawa Hospital Research Institute (OHRI).

Single EDL myofiber isolation and culture—Single myofibers were isolated as previously published by Brun *el al* (Brun et al., 2018), with some modifications to ensure rapid isolation and preservation of muscle stem cells at a nearly quiescent state for the set time point of T=0hrs (Figure S3A confirming only a minor level of activation as demonstrated by low percentage of MyoD+ cells at T=0hrs). Culturing of myofibers allows the natural process of MuSC activation (see Figure S3A for validation of MuSC activation as Pax7+/MyoD+ cells at 4hrs in culture). Briefly, the Extensor Digitorum Longus (EDL) muscle was harvested immediately following cervical dislocation and digested in 0.5% (w/v) Collagenase B (Roche 11088815001) for 35-40 minutes in a 37°C water bath. The EDL muscle was then gently triturated in wash media (Dulbecco's Modified Eagle's Medium (DMEM) containing 4.5 g/L glucose and 1% (v/v) penicillin-streptomycin) to release single myofibers. Single EDL myofibers were then washed twice in wash media to remove excess debris attached to the myofibers. Myofibers were allowed to rest for only 10 min to maintain a semi-quiescent state, before fixing in 2% (w/v) PFA (warmed to 37°C) for 10 min at room temperature. T=0hrs indicates the fixation of myofibers immediately after harvesting. Single EDL myofibers to be cultured were placed in a 24-well plate containing single EDL myofiber culture media (DMEM 4.5 g/L glucose, 20% (v/v) FBS, 1% (v/v) chicken embryo

extract, 1% (v/v) penicillin-streptomycin, 7.5 ng/mL bFGF). Cultured EDL myofibers were incubated in at 37°C, 5% CO_2 between 4-96 hrs, depending on the experimental design. Single EDL myofibers were treated with 2 μM Mdivi-1 (Millipore Sigma; M0199), 10 μM MitoTEMPO (Millipore Sigma; SML0737), 10 or 50 μM BSO (Millipore Sigma; B2515), 10 nM (low dose) or 50 μM Rotenone (Millipore Sigma; R8875), 25nM (low dose) mito-Paraquat (Abcam, ab146819), 1 mM L-Glutathione (GSH) (Millipore Sigma; G4251), 5 mM L-Cysteine (Millipore Sigma; 5360), 5 mM Glycine (Bio-Rad; 1610717), 50 μM Antimycin A (Millipore Sigma; A8674), 5 μM Oligomycin (Millipore Sigma; O4876), 20 nM Rapamycin (Invivogen; tlrl-rap), 10 nM Torin-1 (Invivogen; inh-tor1), 40 ng/mL Recombinant Mouse HGF-A (R&D Systems; 1200-SE) or 10 ng/mL Recombinant human active HGF (Abcam; Ab632), depending on experimental design. Low dose Rotenone (10nM) or mito-Paraquat (25nM) was used to increase mtROS; mitoTEMPO (10 μM) was used to decrease mtROS; exogenous reduced-GSH or the GSH precursor cysteine was used to increase intracellular GSH levels; BSO was used to reduce intracellular GSH levels (Figure S5E,K,O,P). High dose Rotenone (50 μM), Antimycin A (50 μM) and Oligomycin in Figure S6N,O were used to promote mitochondrial dysfunction by inhibiting ETC Complex-1, Complex-III or Complex-V, respectively.

Myoblast cell line and primary myoblast cultures—C2C12 murine myoblasts were cultured in Dulbecco's Modified Eagle's Medium containing 4.5 g/L glucose, supplemented with 10% FBS (v/v) and 1% penicillin-streptomycin (v/v). C2C12s at 50% confluency were treated with 10 nM Rotenone, 1 mM GSH, 10 μM BSO, or 10 μM Mdivi-1 for 24 hrs. Primary myoblasts used for mtROS assessment and gene expression analysis were cultured at 60% confluency in Ham's F-10 containing 20% FBS (v/v), 1% penicillin-streptomycin (v/v) and 2.5ng/uL bFGF. See Figure S5G for validation of primary myoblast population.

Compounds	Company/Cat no.	Concentration
Mdivi-1	Sigma M0199	2 μM
MitoTEMPO	Sigma SML0737	10 μM
L-Buthionine Sulphoxamine (BSO)	Sigma B2515	10 μM
Rotenone	Sigma R8875	10 nM-1 μM
mito-Paraquat (mitoPQ)	Abcam ab146819	25 nM
L-Glutathione (GSH)	Sigma G4251	1 mM
L-Cysteine	Sigma 5360	5 mM
Glycine	Bio-Rad 1610717	5 mM
Antimycin A	Sigma A8674-50MG	50 μM
Oligomycin	Sigma O4876-25MG	5 μM
Rapamycin	Invivogen (tlrl-rap)	20 nM
Torin-1	Invivogen (inh-tor1)	10 nM
Recombinant Mouse HGF-A	R&D Systems 1200-SE	40 ng/mL
Recombinant Human HGF Protein (Active form)	Abcam/ Ab632	10 ng/mL

METHOD DETAILS

Muscle injury—Mice were injected subcutaneously with Buprenorphine (0.1 mg/Kg) and anesthetized by gas inhalation 30 min prior to Cardiotoxin injection. 50 μL of 10 μM Cardiotoxin diluted in phosphate buffered saline (PBS) was injected into the Tibialis Anterior (TA) muscle using a 28G-1/2 insulin syringe. The Cardiotoxin-injected limb was used as the injured muscle, while the contralateral limb received no injection and was used as the uninjured contralateral control. For triple CTX injury performed for OPA1-OE experiments, mice were subjected to three consecutive rounds of CTX-induced injury and repair to the TA muscle, to test the maintenance capacity of MuSCs *in vivo* (see Figure S7H for paradigm). For all CTX treatments, mice recovered in a cage with a heating pad and were monitored 24 hrs post-Cardiotoxin injection. Mice were euthanized by cervical dislocation and TA muscles were dissected and harvested immediately at the desired time-point post-CTX injection. Uninjured mice were used for analysis of intact TA muscles. For the triple CTX experiments, analysis was performed following the last round of muscle repair (21DPI following last CTX injury).

Muscle tissue preparation—At the time of harvest, TA muscles was dissected following cervical dislocation and immediately dropped in 5 mL freshy prepared cold 2% (w/v) PFA (Sigma P6148) and fixed for 30 min, shaking on ice. Following fixation, TA muscles were washed twice with 5 mL of 1x PBS for 5 min, followed by two washes in 5 mL of 0.25 M glycine (dissolved in 1x PBS) for 10 min. TA muscles were then submerged in 5 mL of 5% (w/v) sucrose in a centrifuge tube for 2 hrs at 4°C. TA muscles were transferred to a 1.5 mL centrifuge tube and submerged in 20% sucrose (w/v) for 2-3 days at 4°C. TA tissue was embedded in Optimal Cutting Temperature (OCT) compound (VWR CA95057-838) and frozen in isopentane, cooled using liquid nitrogen for 30 sec, and immediately stored at −80°C. Tissue was sectioned in a cross-sectional orientation at a thickness of 14 μm using the HM525NX Cryostat (University of Ottawa Histology Core) at −28°C onto a charged slide (Fisher Scientific 12-550-15). Slides were stored at −80°C until further processing.

Hematoxylin and Eosin Staining—Tissue sections were stained with Hematoxylin and Eosin (H&E) at the Histology Core Facility at the University of Ottawa. H&E stained tissue sections were imaged using the EVOS F1 Auto2 microscope. Images of entire tissue sections were obtained using a tiling function, whereby single images taken at 20x magnification were stitched together. Quantification of myofiber numbers and size (cross-sectional area, CSA) were measured using the Fiji (ImageJ) software. For quantification of myofiber number following CTX-injury, the number of centrally-nucleated myofibers within a given region of interest (ROI) were counted and normalized to the ROI area (μm^2). For myofiber quantifications in uninjured conditions, the number of peripherally-nucleated myofibers were counted. At least three ROIs were quantified for each section. For myofiber CSA, the myofiber perimeter was traced using the Fiji software drawing tool to measure the minimum Feret diameter. The following equation was used to calculate the CSA based on πr^2, CSA=3.14*(minimum ferret diameter/2)^2.

Immunofluorescence

Tissue sections: TA muscle tissue sections were subjected to antigen retrieval in sodium citrate buffer (10 mM sodium citrate, 0.05% Tween-20) at pH=6.0, followed by 1 hr blocking in 3% (w/v) BSA. Primary antibody was diluted in 3% BSA. 40 μL of diluted primary antibody was added to each tissue section and incubated overnight at 4°C. Primary antibodies include Pax7 (1:13, DHSB PAX7-S), MyoD (1:100, SantaCruz sc-32758), MyoG (1:100, DHSB FD5), Laminin (1:1000, Abcam Ab-11575), Ki67 (Ab-15580). Following primary antibody incubation, tissue slides were washed 5 times for 2 minutes in 40uL of 1xPBS. For primary antibodies raised in mouse, tissue sections were incubated for 30 minutes at room temperature in Biotin (1:250, Jackson Immunoresearch, 115-065-205 diluted in 3% BSA. Following Biotin incubation, tissue sections were washed 5 times for 2 min in 40 μL of 1x PBS. Secondary antibody containing Strepdavidin conjugated Cy3 (1:250 Jackson Immunoresearch, 016-160-084) for primary antibodies raised in mouse, and/or fluorescence-conjugated secondary antibody, including AlexaFluoro 488 (1:500 Invitrogen A11008), and AlexaFluoro 594 (1:500, A11005), and DAPI (1:1000, Sigma D9542) were diluted in 3% BSA and added in 40 μL drops to sections and incubated for 15 min at room temperature. Sections were washed 5 times for 2 min in 40 μL of 1x PBS and slides were mounted using Immu-mount (ThermoFisher 9990402). Immunostained slides were imaged (see microscopy section) and quantified using the Fiji (ImageJ) software. For quantifications of cell populations, the number of positive cells were quantified within a given region of interest (ROI) and normalized to the number of nuclei (DAPI) or the unit area (in μm^2). A minimum of three ROIs were used for all quantifications.

Single EDL myofibers: Single myofibers were permeabilized in 0.1% (v/v) Triton-X and 100 mM glycine, followed by blocking in blocking solution (5% (v/v) horse serum, 2% (w/v) BSA and 0.1% (v/v) Triton-X in PBS) for 5 hours at room temperature. Primary antibody was diluted in blocking solution then added to myofibers at a volume of 100 μL and incubated overnight at 4°C. Primary antibodies include mouse Pax7 (1:13, DHSB PAX7-S), rabbitPax7 (1:100, Thermo Fisher Scientific Pa1-117), mouse MyoD (1:100, SantaCruz sc-32758), mouse MyoG (1:100, DHSB FD5), rabbit Ki67 (1:1000, ab15580), chicken GFP (1:1000 Abcam ab13790) to detect Pax7-GFP, rabbit Tom20 (1:500, ProteinTech 11802-1-AP), rabbit pS6 (1:1000, Cell Signalling Technology 4857S), mouse anti-GSH (1:75, Abcam ab19534), rabbit anti-GSH (1:100, Abcam ab9443), rabbit pRb (1:1000, Cell Signalling Technology 8516S), mouse Cytochrome C (1:500, BD Biosciences 556432). Secondary antibodies, including Cy3 (1:1000, Jackson 715-165-150), AlexaFluoro 488 (1:1000, Thermo Fisher Scientific A11001) were added for 1 hour at room temperature, and then EDL myofibers were mounted using Immumount (ThermoFisher, 9990402) on a charged glass slide (Fisher Scientific, 12-550-15). Glutathione staining intensity was measured by Corrected Total Cell Fluorescence (CTCF) using Fiji (ImageJ).

Antibody Name	Company/Cat no.	Dilution	Assay
Pax7 (mouse)	DHSB PAX7-S	1:13	IF Primary
Pax7 (rabbit)	Thermo Fisher Scientific PA1-117	1:50	IF Primary

Antibody Name	Company/Cat no.	Dilution	Assay
Tom20 (rabbit)	ProteinTech 11802-1-AP	1:500	IF Primary
MyoD (mouse)	SantaCruz sc-32758	1:100	IF Primary
MyoG (mouse)	DHSB FD5	1:100	IF Primary
Laminin (rabbit)	Abcam AB-11575	1:1000	IF Primary
Ki67 (rabbit)	Abcam AB-15580	1:1000	IF Primary
eMHC (mouse)	DHSB F1.652-s	1:15	IF Primary
pS6 (rabbit)	Cell Signalling Technology 4857S	1:1000	IF Primary
pRb (rabbit)	Cell Signalling Technology 8516S	1:1000	IF Primary
Cytochrome C (mouse)	BD Biosciences	1:500	IF Primary
GFP (chicken)	Abcam ab13970	1:1000	IF Primary
GSH (mouse)	Abcam ab19534	1:75	IF Primary
GSH (rabbit)	Abcam ab9443	1:100	IF Primary
Alexa-Fluoro 488 Rabbit	Molecular Probes A11008	*1:500-1:1000	IF Secondary
Alexa-Fluor 488 Mouse	Thermo Fisher Scientific A11001	*1:500-1:1000	IF Secondary
Alexa-Fluor 488 Chicken	Jackson 703-545-155	*1:500-1:1000	IF Secondary
Alexa-Fluor 647 Rabbit	Abcam ab150075	*1:500-1:1000	IF Secondary
Alexa-Fluor 647 Mouse	Abcam ab150107	*1:500-1:1000	IF Secondary
Alexa-Fluor 594 (Rabbit or Mouse)	Thermo Fisher Scientific A11005	*1:500-1:1000	IF Secondary
Cy3 Rabbit	Jackson 711-165-152	1:1000	IF Secondary
Cy3 Mouse	Jackson 715-165-150	1:1000	IF Secondary
Biotin	Jackson 115-065-205	1:250	IF Secondary
Cy3-Conjugated Streptavidin	Jackson 016-160-084	1:250	IF Secondary

*1:500 concentration is used for tissue immunofluorescence staining and 1:1000 is used for single EDL myofiber immunofluorescence staining.

TUNEL assay—Assessment and quantification of apoptosis based on labelling of DNA strand breaks was performed by TUNEL assay (Roche 11684795910) as per the manufacturer's instructions. Briefly, EDL myofibers were isolated and fixed immediately (t=0h fibers) or cultured (t=48h) as previously described. EDL fibers were fixed in 2% PFA and permeabilized for 10 minutes and washed in PBS 3x5 minutes. Following permeabilization, the TUNEL reaction mixture was freshly prepared, and 50μl of reaction mixture was added to each well. The reaction then took place at 37 degrees Celsius for 60 minutes in the dark. Following the reaction, fibers were washed twice in PBS for 5 minutes each. The fibers were then stained with mouse Pax7 antibodies as described. For negative control, prior to the TUNEL reaction, fibers were treated with 0.5μM DNAse solution (Qiagen 79254) for 10 minutes at room temperature.

Microscopy—Stained tissue sections and single EDL myofibers were imaged on an Epifluorescent microscope (Zeiss AxioObserver.Z1). For tissue section imaging, tile scans were used to obtain an image of the entire section. EDL myofibers cultured for 72 hours were imaged using z-stacks to obtain a complete image of cell clusters. EDL myofibers

stained for Tom20 (mitochondrial length measurements) were imaged on the LSM880 Airyscan Confocal Microscope at the uOttawa Cell Biology Image Acquisition Core.

Electron microscopy (EM) analysis of muscle stem cells—Muscle stem cells were isolated by FACS and pelleted at 4200rpm for 2 minutes. Supernatant was removed and 1mL of sterile PBS was added and cells were further pelleted at 1500rpm for 5 minutes. Supernatant was aspirated and 500µl of EM fixative (2.5% glutaraldehyde solution in 0.2M Sodium Cacodylate buffer) was added very carefully so as not to disturb the pellet. Cells were incubated with the EM fixative for 15 minutes at 4°C. Following incubation, cells were centrifuged at 5000rpm for 8 minutes. Supernatant was removed and another 500µl of EM fixative was added. Next, 4% agarose was prepared by adding 0.04g of low-melt agarose to 1mL of 1xTAE and was dissolved by mixing with a pipette and heating in a water bath at 67°C until the agarose was fully dissolved. Cell pellets were warmed in their centrifuge tubes to 37°C on a heating block. Next, 30µl of 4% agarose was quickly added to the cell pellet and was gently resuspended, before centrifuging at 2500rpm for 3 minutes. The agarose-embedded pellet was incubated at 4°C for 10 minutes. Following 10 minutes, 500µl of EM fixative was added to the tube, and the pellet was very carefully removed from the wall of the tube so that it remained free-floating. Agarose-embedded samples were then sent to the Facility for Electron Microscopy Research at McGill University for processing and sectioning. Sections were then imaged at the University of Ottawa TEM core facility using a EM-1400Plus TEM. Cristae analysis was performed using FIJI and a minimum of 100 mitochondria were analysed. For each individual cristae, the average diameter was measured from three representative regions.

Mitochondrial length and volume measurements—Mitochondria were stained with the outer mitochondrial membrane protein Tom20 and imaged using Airyscan Confocal Microscopy at the Cell Biology Image Acquisition Core Faculty at uOttawa. Mitochondrial length was measured by creating 2D projections using Fiji (ImageJ) software and manually tracing the mitochondria. Mitochondrial length was either binned into different categories or taken as an average as previously described (Khacho et al., 2016). Distribution dot plots were generated in Prism and bars represent the mean of all data points. 3D mitochondrial images were reconstructed using the Imaris Filaments application, or captured using the Imaris 3D viewer. Individual mitochondrial volume measurements were performed using Prism by generating surface rendering

RNA isolation and qPCR—Total RNA was isolated from freshly isolated muscle stem cells using the PicoPure RNA isolation kit (ThermoFisher, KIT0214). Myoblast and whole muscle RNA was isolated using Trizol-based extraction (Trizol, ThermoFisher 15596026). RNA extractions were performed under RNAse free conditions and preserved at −80 °C. RNA was quantified using the Nanodrop 2000 spectrophotometer. qPCR was then performed using the Rotor-Gene SYBR RT-QPCR kit (Qiagen, 204174). Each sample was run in triplicate using the following thermal cycler programming: 55°C for 10 minutes, 95°C for 5 minutes, cycling of 95°C for 5 seconds and 60°C for 10 seconds for 40 repeat cycles, melting from 60-95°C with a 1°C rise each step with 90 seconds of pre-melt conditioning on the first step and 5 seconds for each subsequent step, as previously described (Khacho et al.,

2016). Every qPCR run was performed alongside a housekeeping gene (GAPDH, β-Actin and/or β-Tubulin) for normalization. See Figure S3L for validation of qPCR normalization using β-Actin and β-Tubulin as housekeeping genes. Each gene was fitted to the appropriate standard curve and subsequently analysed. All qPCR analysis was normalized to GAPDH unless otherwise stated.

Immunoblot—For total cell lysates, cells were washed with phosphate-buffered saline (PBS), lysed with 4% SDS in PBS, boiled for 5 minutes and the DNA was sheared by passage through a 26- gauge needle. Primary antibodies recognizing OPA1 (Abcam; ab42364) and GAPDH (Abcam; ab8245) were used. Ponceau staining was used to ensure equal protein loading for lysates derivied from MuSCs. A secondary antibody conjugated to horseradish peroxidase (Jackson ImmunoResearch) was used and detected by Western Lightning Chemiluminescence Reagent Plus (Perkin Elmer).

ATP Assay—Muscle stem cells were plated in suspension in a 96-well black transparent F-bottom microplate (LifeSciences, 781611) and treated with or without 20 μM Oligomycin for 30 min to block the activity of ATP synthase and thus mitochondrial oxidative phosphorylation (to observe OXPHOS-dependent ATP generation). ATP levels were then detected using the CellTiterGlo cell viability assay kit (Promega, G9241). ATP concentrations were retrieved based on a standard curve analysis. Cell counts and viability were performed to allow for normalization of data using a hematocytometer and Trypan Blue to identify dead cells.

Oxygen Consumption (OCR) and Extracellular Acidification Rate (ECAR)—The Seahorse XF96 Extracellular Flux Analyzer (Seahorse Biosciences) was used to measure oxygen consumption and extracellular acidification rate in cells. Briefly, MACS isolated muscle stem cells from OPA1-WT and OPA1-MKO animals were seeded onto Matrigel coated 96-well Seahorse plates at a density of $1.5x10^5$ cells/well. For measurements performed immediately after isolation (T=0 hours), cells were seeded in 175 L of Seahorse media (4.15g DMEM powder, 0.925g NaCl, 2.25 g glucose, 5 mL of 200 mM L-glutamine, 5 mL of 100 mM Na-pyruvate, 490 mL H2O, pH 7.4) and plates were immediately spun at 200 x g for 1 minute and allowed to stop without brakes. For measurements performed at T=24 hours, muscle stem cells were cultured for 24 hours in 150 μL muscle stem cell culture media and kept in normal cell-incubation conditions. Prior to the assay, cells were washed twice in 1x PBS and placed in 175 μL of Seahorse Media. Plates were placed in a CO2 free incubator, at 37 °C for 1 hour prior to loading into the XF Analyzer. Following measurement of basal respiration, cells were treated sequentially with oligomycin (1.0 μM), FCCP (2 μM) and of Rotenone and Antimycin A (0.5 μM). Each measurement was taken over a 3-minute interval followed by 3 minutes of mixing. Three measurements were taken for each respiratory state. Immediately following completion of the assay, media from wells was removed and cells were washed in 1xPBS. 50 μL of RIPA buffer was added to each well and plates were frozen at −20°C overnight. Protein concentration was subsequently measured using a BCA assay. All Seahorse values were normalized to the appropriate protein levels and quantified.

MitoSOX staining—Mitochondrial ROS (mtROS) in muscle stem cells was measured using the MitoSOX assay as previously published (Khacho et al., 2016; Thumiah-Mootoo et al., 2021). Briefly, muscle stem cells were isolated by MACS. Before staining, 50 μM Rotenone was added for 10 min at 37°C to induce mtROS as a positive control. 5 μM MitoSOX Red (Thermo Fisher Scientific M36008) was added to each sample and incubated for 15 min at 37°C. Samples were washed in PBS buffer and then resuspended in 300 μL of PBS and mtROS was measured by Flow Cytometry at the Flow Cytometry Core Facility at the University of Ottawa. Data were analyzed as mean fluorescence intensity using the FlowJo Software. For MitoSOX on MuSCs residing on myofibers, single EDL myofibers were isolated as previously described and placed in EDL culture media. 5 μM MitoSOX Red was added to each sample and incubated for 15 minutes at 37°C. Samples were washed in 1xPBS containing 1 μM Hoescht 33342. EDL myofibers were mounted using Immumount (ThermoFisher 9990402) on a charged glass slide. Data were analyzed as corrected total cell fluorescence (CTCF) using Fiji (ImageJ) (CTCF= IntDen – (Area of selected cell X Mean fluorescence of background readings). See Figure S5D,E for validation of mtROS assessment by MitoSOX in MuSCs by Flow cytometry and microscopy, respectively.

***In vivo* EdU injection—**EdU was prepared (Baseclick EdU, BCN-001-500) and injected 15 hours prior to muscle harvest. EdU detection *in vivo* was performed using the BaseClick EdU detection kit (Sigma, BCK647-IV-IM-M). For *in vivo* EdU experiments in Figure 2S,T,U, OPA1-WT and OPA1-MKO animals were injured in one limb, followed by an EdU injection 15hrs before harvesting TA muscle from the contralateral limb at 4DPI, to label cells that enter the cell cycle. For experiments in Figure 2D and Figure 3F, OPA1-WT and OPA1-MKO animals were subjected to injury in the TA muscle, followed by an EdU injection 15hrs before harvesting the injured TA muscle at 2DPI or 4DPI.

***In vitro* EdU pulse—**Single EDL fibers were isolated as previously described and cultured in EDL culture media for 24 hours. 1 hour prior to harvest, 500 μL of culture was removed from each well, and 500 μL of pre-warmed culture media containing 20 μM EdU dissolved in DMSO was added, at a final concentration of 10 μM EdU per well. Fibers were left to incubate with 10 μM EdU for 1 hour and the harvested and fixed in 2% PFA. Fibers were then permeabilized and blocked as previously described. Prior to primary antibody staining, the EdU detection reaction was carried out using the BaseClick EdU detection kit (Sigma, BCK647-IV-IM-M) following the manufacturer's protocol. Briefly, 500 μLof the reaction cocktail was added to each well and the reaction took place on a rocker protected from darkness at room temperature for 30 minutes. Following this, fibers were washed in PBS 3x5 minutes and proceeded to primary antibody staining.

***In vivo* HGFA Injections—**Recombinant HGFA (R&D Systems; 1200-SE) was administered to mice at a dose of 1 μg diluted in 200 μL PBS via tail vein injection as previously published (Rodgers et al., 2017). Vehicle control injections were administered by tail vein injection using 200 μL of PBS. Mice were sacrificed two days following HGFA injection and the EDL muscle was isolated to assess muscle stem cells on single EDL myofibers.

***In Vivo* mitoTEMPO treatments—**For *in vivo* rescue of OPA1-MKO phenotype with mitoTEMPO, 7-8 week old OPA1-WT and OPA1-MKO were used. mitoTEMPO was administered to OPA1-MKO mice at a dose of lmg/kg/day, diluted in 1xPBS, via intraperitoneal (IP) injection. Equal volumes of 1xPBS were IP injected into OPA1-WT and OPA1-MKO mice to serve as saline control. See Figure S5N for the experimental paradigm. Briefly, mitoTEMPO injections began at the start of Tamoxifen treatment and persisted until animals were sacrificed. 3 days after the cessation of Tamoxifen treatment, OPA1-WT and OPA1-MKO mice underwent CTX injury to one limb. 15hrs prior to tissue collection, EdU was administered to all mice (see above for in vivo EdU injection details). Tissue collection occurred at 2DPI. Injured TA muscles were harvested for cross-section immunofluorescence analysis, whereas the EDL muscle from the contralateral limbs was isolated and fixed immediately (T=0hrs) for further analysis.

GDF-15 and FGF-21 ELISA—Blood was extracted from mice prior to sacrifice by ventricular puncture and immediately placed in EDTA-coated tubes (Sarstedt, 41.1395.105). Blood was then spun at 2000g for 15 minutes at room temperature. The supernatant (plasma) was carefully removed, placed in a 1.5mL tube and stored at −80°C until further analysis. GDF-15 levels in plasma were measured via Abcam Mouse GDF-15 SimpleStep ELISA Kit (Ab216947) and FGF-21 levels in plasma were measured via Millipore Rat/Mouse Fibroblast Growth Factor-21 ELISA Kit (EZRMFGF21-26K) according to the manufacturer's instructions.

RNAseq analysis—Muscle stem cells were isolated by FACS from acute OPA1-WT and OPA1-MKO animals (3 days after last TAM administration) and pelleted at 4200rpm for 2 minutes. Total RNA was isolated from freshly isolated muscle stem cells using the PicoPure RNA isolation kit (ThermoFisher, KIT0214). RNA extractions were performed under RNAse free conditions and preserved at −80 °C. RNA was quantified using the Nanodrop 2000 spectrophotometer and RNA quality assessment was performed by fragment anlaysis at the Ottawa Hospital StemCore Facility. Only samples with RIN > 8 were utilized. RNAseq library preparation and sequencing were conducted by the he Centre for Applied Genomics at The Hospital for Sick Children (Toronto, Canada). From each sample, about 40-50 million reads were obtained using NovaSeq. To identify differentially expressed genes, high stringency parameters were used whereby 1) we removed all genes where 3 or more samples had FPKM values <1, and 2) only transcripts with log fold change values ≥1 or ≤−1 and adjusted P value ≤ 0.05 were included in the analysis. GO analysis of the significantly changed genes was performed using the DAVID database. Heat maps were generated using Morpheus-Broad Institute.

Data mining—Available micro-array and RNAseq datasets were retrieved from the public Gene Expression Omnibus (GEO) repository (http://www.ncbi.nlm.nih.gov/geo) website under Accession Numbers GSE47177 (Liu et al., 2013), GSE63860 (Alonso-Martin et al., 2016), GSE50821 (Sinha et al., 2014) and GSE121589 (Shcherbina et al., 2020). GEO2R was used to compute the data sets and obtain Log2FC and adj.p-values. Gene Ontology terms for differentially expressed genes was acquired using the NIH DAVID database.

MolBioTools was used for comparative analysis of differentially expressed genes from the different acquired datasets. Heat maps were generated using Morpheus.

QUANTIFICATION AND STATISTICAL ANALYSIS

Statistical Analyses—Statistical tests were determined and computed with Excel (Student's paired and unpaired t-tests) or Prism GraphPad (one-way, two-way or repeated measure ANOVAs with respective Post-HOC analyses). All statistics are presented with the following significance: $p<0.05$ *, $p<0.01$ **, $p<0.001$ ***.

- Figure 1, statistical analysis was performed using Two-way ANOVA with Neuman-Keuls Post-HOC Test (Figure 1B,C) and Student's t-test (Figure 1E,G,L).
- Figure 2, statistical analysis was performed using Student's t-test.
- Figure 3, statistical analysis was performed using Student's t-test for all with the following exception: Two-way ANOVA with Neuman-Keuls post-HOC test (Figure 3B,G), or Tukey's (Figure 3S) Post-HOC test.
- Figure 4, statistical analysis was performed using Student's t-test (Figure 4H,I,K,L), One-Way ANOVAs with Dunnett's (Figure 4A,C,D,M) or Tukey's Post-HOC test (Figure 4E,F,N).
- Figure 5, statistical analysis was performed using Student's t-test for all with the following exception: One-way ANOVAs with Tukey's Post-HOC test (Figure 5F,G,H,L,M,Q)
- Figure 6, statistical analysis was performed using Student's t-test for all with the following exception: One-way ANOVAs with Tukey's Post-HOC test (Figure 6M,P-S).
- Figure 7, statistical analysis was performed using Student's t-test for all with the following exception: One-way ANOVAs with Tukey's Post-HOC test (Figure 7M,S).

Supplementary Material

Refer to Web version on PubMed Central for supplementary material.

Acknowledgments

This work was supported by funds from Canada Research Chair (CRC), CIHR, Stem Cell Network and J.P. Bickell to MK, and NSERC-CGSM to SW. We thank Nikita Larionov for mouse colony management and all animal procedures; Vera Tang and Fernando Ortiz at uOttawa and OHRI Flow cytometry facilities for expert advice; and Louise Pelletier Histology Core; Lavin Kazemi for genotyping assistance and Katherine Manta for some technical support.

Inclusion and diversity

We worked to ensure sex balance in the selection of non-human subjects. One or more of the authors of this paper self-identifies as an underrepresented ethnic minority in science. One

or more of the authors of this paper self-identifies as a member of the LGBTQ+ community. One or more of the authors of this paper self-identifies as living with a disability.

References

Almada AE, and Wagers AJ (2016). Molecular circuitry of stem cell fate in skeletal muscle regeneration, ageing and disease. Nat Rev Mol Cell Biol 17, 267–279.10.1038/nrm.2016.7. [PubMed: 26956195]

Alonso-Martin S, Rochat A, Mademtzoglou D, Morais J, de Reyniès A, Auradé F, Chang TH, Zammit PS, and Relaix F (2016). Gene Expression Profiling of Muscle Stem Cells Identifies Novel Regulators of Postnatal Myogenesis. Front Cell Dev Biol 4, 58. 10.3389/fcell.2016.00058. [PubMed: 27446912]

Amartuvshin O, Lin CH, Hsu SC, Kao SH, Chen A, Tang WC, Chou HL, Chang DL, Hsu YY, Hsiao BS, et al. (2020). Aging shifts mitochondrial dynamics toward fission to promote germline stem cell loss. Aging Cell, e13191. 10.1111/acel.13191. [PubMed: 32666649]

Anderson CJ, Kahl A, Fruitman H, Qian L, Zhou P, Manfredi G, and Iadecola C (2020). Prohibitin levels regulate OMA1 activity and turnover in neurons. Cell Death Differ 27, 1896–1906. 10.1038/s41418-019-0469-4. [PubMed: 31819158]

Ansó E, Weinberg SE, Diebold LP, Thompson BJ, Malinge S, Schumacker PT, Liu X, Zhang Y, Shao Z, Steadman M, et al. (2017). The mitochondrial respiratory chain is essential for haematopoietic stem cell function. Nat Cell Biol 19, 614–625. 10.1038/ncb3529. [PubMed: 28504706]

Blanpain C, Lowry WE, Geoghegan A, Polak L, and Fuchs E (2004). Self-renewal, multipotency, and the existence of two cell populations within an epithelial stem cell niche. Cell 118, 635–648. 10.1016/j.cell.2004.08.012. [PubMed: 15339667]

Blau HM, Cosgrove BD, and Ho AT (2015). The central role of muscle stem cells in regenerative failure with aging. Nat Med 21, 854–862. 10.1038/nm.3918. [PubMed: 26248268]

Brack AS, Conboy MJ, Roy S, Lee M, Kuo CJ, Keller C, and Rando TA (2007). Increased Wnt signaling during aging alters muscle stem cell fate and increases fibrosis. Science 317, 807–810. 10.1126/science.1144090. [PubMed: 17690295]

Brun CE, Wang YX, and Rudnicki MA (2018). Single EDL Myofiber Isolation for Analyses of Quiescent and Activated Muscle Stem Cells. Methods Mol Biol 1686, 149–159. 10.1007/978-1-4939-7371-2_11. [PubMed: 29030819]

Buck MD, O'Sullivan D, Klein Geltink RI, Curtis JD, Chang CH, Sanin DE, Qiu J, Kretz O, Braas D, van der Windt GJ, et al. (2016). Mitochondrial Dynamics Controls T Cell Fate through Metabolic Programming. Cell 166, 63–76. 10.1016/j.cell.2016.05.035. [PubMed: 27293185]

Carlson ME, Hsu M, and Conboy IM (2008). Imbalance between pSmad3 and Notch induces CDK inhibitors in old muscle stem cells. Nature 454, 528–532. 10.1038/nature07034. [PubMed: 18552838]

Chakkalakal JV, Jones KM, Basson MA, and Brack AS (2012). The aged niche disrupts muscle stem cell quiescence. Nature 490, 355–360. 10.1038/nature11438. [PubMed: 23023126]

Chandel NS, Jasper H, Ho TT, and Passegué E (2016). Metabolic regulation of stem cell function in tissue homeostasis and organismal ageing. Nat Cell Biol 18, 823–832. 10.1038/ncb3385. [PubMed: 27428307]

Cheung TH, and Rando TA (2013). Molecular regulation of stem cell quiescence. Nat Rev Mol Cell Biol 14, 329–340. 10.1038/nrm3591. [PubMed: 23698583]

Cho IJ, Lui PP, Obajdin J, Riccio F, Stroukov W, Willis TL, Spagnoli F, and Watt FM (2019). Mechanisms, Hallmarks, and Implications of Stem Cell Quiescence. Stem Cell Reports 12, 1190–1200. 10.1016/j.stemcr.2019.05.012. [PubMed: 31189093]

Civenni G, Bosotti R, Timpanaro A, Vàzquez R, Merulla J, Pandit S, Rossi S, Albino D, Allegrini S, Mitra A, et al. (2019). Epigenetic Control of Mitochondrial Fission Enables Self-Renewal of Stem-like Tumor Cells in Human Prostate Cancer. Cell Metab 30, 303–318.e306. 10.1016/j.cmet.2019.05.004. [PubMed: 31130467]

Del Campo A, Contreras-Hernández I, Castro-Sepúlveda M, Campos CA, Figueroa R, Tevy MF, Eisner V, Casas M, and Jaimovich E (2018). Muscle function decline and mitochondria changes in

middle age precede sarcopenia in mice. Aging (Albany NY) 10, 34–55. 10.18632/aging.101358. [PubMed: 29302020]

Dumont NA, Wang YX, and Rudnicki MA (2015). Intrinsic and extrinsic mechanisms regulating satellite cell function. Development 142, 1572–1581. 10.1242/dev.114223. [PubMed: 25922523]

Eliazer S, Muncie JM, Christensen J, Sun X, D'Urso RS, Weaver VM, and Brack AS (2019). Wnt4 from the Niche Controls the Mechano-Properties and Quiescent State of Muscle Stem Cells. Cell Stem Cell 25, 654–665.e654. 10.1016/j.stem.2019.08.007. [PubMed: 31495781]

Feige P, Brun CE, Ritso M, and Rudnicki MA (2018). Orienting Muscle Stem Cells for Regeneration in Homeostasis, Aging, and Disease. Cell Stem Cell 23, 653–664. 10.1016/j.stem.2018.10.006. [PubMed: 30388423]

Forni MF, Peloggia J, Trudeau K, Shirihai O, and Kowaltowski AJ (2016). Murine Mesenchymal Stem Cell Commitment to Differentiation Is Regulated by Mitochondrial Dynamics. Stem Cells 34, 743–755. 10.1002/stem.2248. [PubMed: 26638184]

Gopinath SD, and Rando TA (2008). Stem cell review series: aging of the skeletal muscle stem cell niche. Aging Cell 7, 590–598. 10.1111/j.1474-9726.2008.00399.x. [PubMed: 18462272]

Heo SJ, Driscoll TP, Thorpe SD, Nerurkar NL, Baker BM, Yang MT, Chen CS, Lee DA, and Mauck RL (2016). Differentiation alters stem cell nuclear architecture, mechanics, and mechano-sensitivity. Elife 5. 10.7554/eLife.18207.

Hu H, and Li M (2016). Mitochondria-targeted antioxidant mitotempo protects mitochondrial function against amyloid beta toxicity in primary cultured mouse neurons. Biochem Biophys Res Commun 478, 174–180. 10.1016/j.bbrc.2016.07.071. [PubMed: 27444386]

Ishihara N, Fujita Y, Oka T, and Mihara K (2006). Regulation of mitochondrial morphology through proteolytic cleavage of OPA1. EMBO J 25, 2966–2977. 10.1038/sj.emboj.7601184. [PubMed: 16778770]

Khacho M, Clark A, Svoboda DS, Azzi J, MacLaurin JG, Meghaizel C, Sesaki H, Lagace DC, Germain M, Harper ME, et al. (2016). Mitochondrial Dynamics Impacts Stem Cell Identity and Fate Decisions by Regulating a Nuclear Transcriptional Program. Cell Stem Cell 19, 232–247. 10.1016/j.stem.2016.04.015. [PubMed: 27237737]

Liu L, Cheung TH, Charville GW, Hurgo BM, Leavitt T, Shih J, Brunet A, and Rando TA (2013). Chromatin modifications as determinants of muscle stem cell quiescence and chronological aging. Cell Rep 4, 189–204. 10.1016/j.celrep.2013.05.043. [PubMed: 23810552]

Lyublinskaya OG, Borisov YG, Pugovkina NA, Smirnova IS, Obidina JV, Ivanova JS, Zenin VV, Shatrova AN, Borodkina AV, Aksenov ND, et al. (2015). Reactive Oxygen Species Are Required for Human Mesenchymal Stem Cells to Initiate Proliferation after the Quiescence Exit. Oxid Med Cell Longev 2015, 502105. 10.1155/2015/502105. [PubMed: 26273423]

Machado L, Esteves de Lima J, Fabre O, Proux C, Legendre R, Szegedi A, Varet H, Ingerslev LR, Barrès R, Relaix F, and Mourikis P (2017). In Situ Fixation Redefines Quiescence and Early Activation of Skeletal Muscle Stem Cells. Cell Rep 21, 1982–1993. 10.1016/j.celrep.2017.10.080. [PubMed: 29141227]

Maryanovich M, Zaltsman Y, Ruggiero A, Goldman A, Shachnai L, Zaidman SL, Porat Z, Golan K, Lapidot T, and Gross A (2015). An MTCH2 pathway repressing mitochondria metabolism regulates haematopoietic stem cell fate. Nat Commun 6, 7901. 10.1038/ncomms8901. [PubMed: 26219591]

Miller I, Min M, Yang C, Tian C, Gookin S, Carter D, and Spencer SL (2018). Ki67 is a Graded Rather than a Binary Marker of Proliferation versus Quiescence. Cell Rep 24, 1105–1112.e1105. 10.1016/j.celrep.2018.06.110. [PubMed: 30067968]

Murphy MM, Lawson JA, Mathew SJ, Hutcheson DA, and Kardon G (2011). Satellite cells, connective tissue fibroblasts and their interactions are crucial for muscle regeneration. Development 138, 3625–3637. 10.1242/dev.064162. [PubMed: 21828091]

Murphy MP (2009). How mitochondria produce reactive oxygen species. Biochem J 417, 1–13. 10.1042/BJ20081386. [PubMed: 19061483]

Oh J, Lee YD, and Wagers AJ (2014). Stem cell aging: mechanisms, regulators and therapeutic opportunities. Nat Med 20, 870–880. 10.1038/nm.3651. [PubMed: 25100532]

Pasut A, Jones AE, and Rudnicki MA (2013). Isolation and culture of individual myofibers and their satellite cells from adult skeletal muscle. J Vis Exp, e50074. 10.3791/50074. [PubMed: 23542587]

Patten DA, McGuirk S, Anilkumar U, Antoun G, Gandhi K, Parmar G, Iqbal MA, Wong J, Richardson RB, St-Pierre J, et al. (2021). Altered mitochondrial fusion drives defensive glutathione synthesis in cells able to switch to glycolytic ATP production. Biochim Biophys Acta Mol Cell Res 1868, 118854. 10.1016/j.bbamcr.2020.118854. [PubMed: 32926942]

Paul MK, Bisht B, Darmawan DO, Chiou R, Ha VL, Wallace WD, Chon AT, Hegab AE, Grogan T, Elashoff DA, et al. (2014). Dynamic changes in intracellular ROS levels regulate airway basal stem cell homeostasis through Nrf2-dependent Notch signaling. Cell Stem Cell 15, 199–214. 10.1016/j.stem.2014.05.009. [PubMed: 24953182]

Price FD, von Maltzahn J, Bentzinger CF, Dumont NA, Yin H, Chang NC, Wilson DH, Frenette J, and Rudnicki MA (2014). Inhibition of JAK-STAT signaling stimulates adult satellite cell function. Nat Med 20, 1174–1181. 10.1038/nm.3655. [PubMed: 25194569]

Rocheteau P, Gayraud-Morel B, Siegl-Cachedenier I, Blasco MA, and Tajbakhsh S (2012). A subpopulation of adult skeletal muscle stem cells retains all template DNA strands after cell division. Cell 148, 112–125. 10.1016/j.cell.2011.11.049. [PubMed: 22265406]

Rodgers JT, King KY, Brett JO, Cromie MJ, Charville GW, Maguire KK, Brunson C, Mastey N, Liu L, Tsai CR, et al. (2014). mTORC1 controls the adaptive transition of quiescent stem cells from G0 to G(Alert). Nature 510, 393–396. 10.1038/nature13255. [PubMed: 24870234]

Rodgers JT, Schroeder MD, Ma C, and Rando TA (2017). HGFA Is an Injury-Regulated Systemic Factor that Induces the Transition of Stem Cells into G. Cell Rep 19, 479–486. 10.1016/j.celrep.2017.03.066. [PubMed: 28423312]

Ryall JG, Dell'Orso S, Derfoul A, Juan A, Zare H, Feng X, Clermont D, Koulnis M, Gutierrez-Cruz G, Fulco M, and Sartorelli V (2015). The NAD(+)-dependent SIRT1 deacetylase translates a metabolic switch into regulatory epigenetics in skeletal muscle stem cells. Cell Stem Cell 16, 171–183. 10.1016/j.stem.2014.12.004. [PubMed: 25600643]

Sambasivan R, Gayraud-Morel B, Dumas G, Cimper C, Paisant S, Kelly RG, Kelly R, and Tajbakhsh S (2009). Distinct regulatory cascades govern extraocular and pharyngeal arch muscle progenitor cell fates. Dev Cell 16, 810–821. 10.1016/j.devcel.2009.05.008. [PubMed: 19531352]

Sayed RK, de Leonardis EC, Guerrero-Martínez JA, Rahim I, Mokhtar DM, Saleh AM, Abdalla KE, Pozo MJ, Escames G, López LC, and Acuña-Castroviejo D (2016). Identification of morphological markers of sarcopenia at early stage of aging in skeletal muscle of mice. Exp Gerontol 83, 22–30. 10.1016/j.exger.2016.07.007. [PubMed: 27435496]

Sebastián D, Palacín M, and Zorzano A (2017). Mitochondrial Dynamics: Coupling Mitochondrial Fitness with Healthy Aging. Trends Mol Med 23, 201–215. 10.1016/j.molmed.2017.01.003. [PubMed: 28188102]

Shcherbina A, Larouche J, Fraczek P, Yang BA, Brown LA, Markworth JF, Chung CH, Khaliq M, de Silva K, Choi JJ, et al. (2020). Dissecting Murine Muscle Stem Cell Aging through Regeneration Using Integrative Genomic Analysis. Cell Rep 32, 107964. 10.1016/j.celrep.2020.107964. [PubMed: 32726628]

Shin CS, Mishra P, Watrous JD, Carelli V, D'Aurelio M, Jain M, and Chan DC (2017). The glutamate/cystine xCT antiporter antagonizes glutamine metabolism and reduces nutrient flexibility. Nat Commun 8, 15074. 10.1038/ncomms15074. [PubMed: 28429737]

Signer RA, and Morrison SJ (2013). Mechanisms that regulate stem cell aging and life span. Cell Stem Cell 12, 152–165. 10.1016/j.stem.2013.01.001. [PubMed: 23395443]

Sincennes MC, Wang YX, and Rudnicki MA (2017). Primary Mouse Myoblast Purification using Magnetic Cell Separation. Methods Mol Biol 1556, 41–50. 10.1007/978-1-4939-6771-1_3. [PubMed: 28247344]

Sinha M, Jang YC, Oh J, Khong D, Wu EY, Manohar R, Miller C, Regalado SG, Loffredo FS, Pancoast JR, et al. (2014). Restoring systemic GDF11 levels reverses age-related dysfunction in mouse skeletal muscle. Science 344, 649–652. 10.1126/science.1251152. [PubMed: 24797481]

Song M, Franco A, Fleischer JA, Zhang L, and Dorn GW (2017). Abrogating Mitochondrial Dynamics in Mouse Hearts Accelerates Mitochondrial Senescence. Cell Metab 26, 872–883.e875. 10.1016/j.cmet.2017.09.023. [PubMed: 29107503]

Tagde A, Singh H, Kang MH, and Reynolds CP (2014). The glutathione synthesis inhibitor buthionine sulfoximine synergistically enhanced melphalan activity against preclinical models of multiple myeloma. Blood Cancer J 4, e229. 10.1038/bcj.2014.45. [PubMed: 25036800]

Tezze C, Romanello V, Desbats MA, Fadini GP, Albiero M, Favaro G, Ciciliot S, Soriano ME, Morbidoni V, Cerqua C, et al. (2017). Age-Associated Loss of OPA1 in Muscle Impacts Muscle Mass, Metabolic Homeostasis, Systemic Inflammation, and Epithelial Senescence. Cell Metab 25, 1374–1389.e1376. 10.1016/j.cmet.2017.04.021. [PubMed: 28552492]

Thumiah-Mootoo M, Podinic T, and Khacho M (2021). Assessment of Mitochondrial Reactive Oxygen Species and Redox Regulation in Stem Cells. Methods Mol Biol 2277, 289–297. 10.1007/978-1-0716-1270-5_18. [PubMed: 34080158]

Tormos KV, Anso E, Hamanaka RB, Eisenbart J, Joseph J, Kalyanaraman B, and Chandel NS (2011). Mitochondrial complex III ROS regulate adipocyte differentiation. Cell Metab 14, 537–544. 10.1016/j.cmet.2011.08.007. [PubMed: 21982713]

Tümpel S, and Rudolph KL (2019). Quiescence: Good and Bad of Stem Cell Aging. Trends Cell Biol 29, 672–685. 10.1016/j.tcb.2019.05.002. [PubMed: 31248787]

van Velthoven CTJ, and Rando TA (2019). Stem Cell Quiescence: Dynamism, Restraint, and Cellular Idling. Cell Stem Cell 24, 213–225. 10.1016/j.stem.2019.01.001. [PubMed: 30735649]

Varanita T, Soriano ME, Romanello V, Zaglia T, Quintana-Cabrera R, Semenzato M, Menabò R, Costa V, Civiletto G, Pesce P, et al. (2015). The OPA1-dependent mitochondrial cristae remodeling pathway controls atrophic, apoptotic, and ischemic tissue damage. Cell Metab 21, 834–844. 10.1016/j.cmet.2015.05.007. [PubMed: 26039448]

Yucel N, Wang YX, Mai T, Porpiglia E, Lund PJ, Markov G, Garcia BA, Bendall SC, Angelo M, and Blau HM (2019). Glucose Metabolism Drives Histone Acetylation Landscape Transitions that Dictate Muscle Stem Cell Function. Cell Rep 27, 3939–3955.e3936. 10.1016/j.celrep.2019.05.092. [PubMed: 31242425]

Zhang Z, Wakabayashi N, Wakabayashi J, Tamura Y, Song WJ, Sereda S, Clerc P, Polster BM, Aja SM, Pletnikov MV, et al. (2011). The dynamin-related GTPase Opa1 is required for glucose-stimulated ATP production in pancreatic beta cells. Mol Biol Cell 22, 2235–2245. 10.1091/mbc.E10-12-0933. [PubMed: 21551073]

Zhong X, Cui P, Cai Y, Wang L, He X, Long P, Lu K, Yan R, Zhang Y, Pan X, et al. (2019). Mitochondrial Dynamics Is Critical for the Full Pluripotency and Embryonic Developmental Potential of Pluripotent Stem Cells. Cell Metab 29, 979–992.e974. 10.1016/j.cmet.2018.11.007. [PubMed: 30527743]

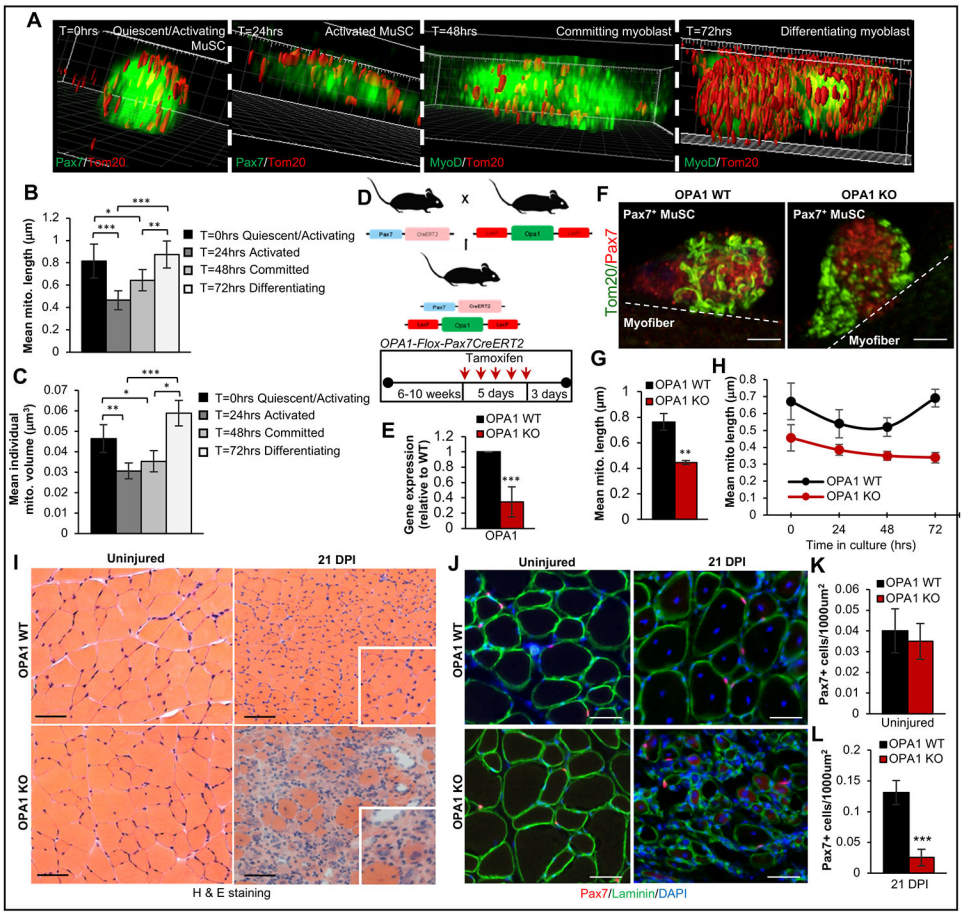

Figure 1. Loss of OPA1 impairs the maintenance and self-renewal of adult muscle stem cells following injury.

(A) Confocal 3D reconstruction images of mitochondria (Tom20) in MuSCs on myofibers.

(B,C) Mitochondrial length (B) and volume (C) in MuSCs on myofibers cultured for 0, 24, 48 and 72hrs. n=≥ 100 mitochondria, 3 independent experiments (ind. exp.), mean ± SEM.

(D,E) Schematic of OPA1-MKO mouse model and TAM paradigm (D) and qPCR (E). n=5 independent biological replicates (ind. biol. rep.), mean ± SD.

(F) 2D projected confocal images of mitochondria (Tom20) in MuSCs on myofibers at T=0hrs. Scale=3µm.

(G,H) Mitochondrial length in MuSCs at T=0hrs (G) or cultured for 0-72hrs (H). n= ≥3 ind. exp.; ≥100 mitochondria, mean ± SEM.

(I) H&E images of TA cross-sections from uninjured and 21DPI regenerated muscle. Scale=50µm.

(J) Immunofluorescence of Pax7 (MuSC), Laminin (muscle), and DAPI (nuclei) in uninjured TA cross-sections and 21DPI following CTX injury. Scale=50µm.

(K,L) Pax7+ cells in uninjured TA and 21DPI following CTX injury. n=4 ind. biol. rep., mean ± SD.

See also Figure S1

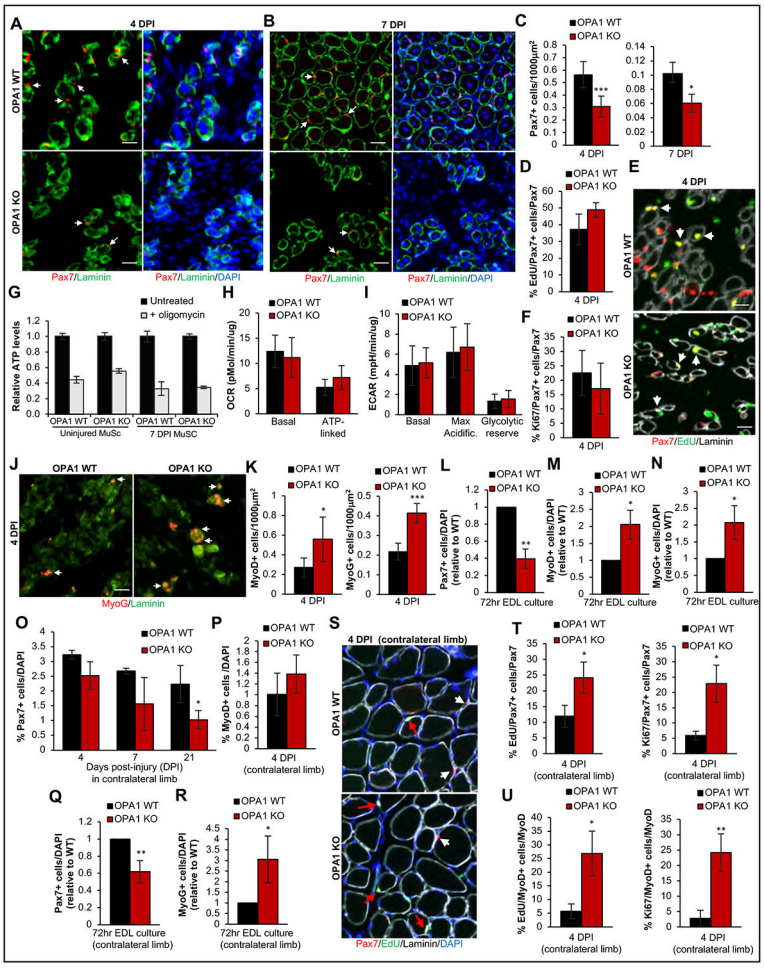

Figure 2. Loss of OPA1 primes the activation and commitment of muscle stem cells.

(A,B) Immunofluorescence of TA cross-sections at 4 and 7DPI following CTX injury. White arrows are Pax7+ cells. Scale=25µm.

(C) Pax7+ cells in TA cross-sections at 4 and 7DPI. n=6 4DPI; n=3 7DPI ind. biol. rep., mean ± SD.

(D) Pax7+ cells incorporating EdU in TA cross-sections at 4DPI. n=4 ind. biol. rep., mean ± SD.

(E) Immunofluorescence of TA cross-sections stained for Pax7, EdU, and Laminin at 4DPI. Arrows are Pax7/EdU+ cells. Scale=25µm.

(F) Pax7+ cells expressing Ki67 in TA cross-sections at 4DPI. n=4 ind. biol. rep., mean ± SD.

(G) ATP levels at steady state (black) and after 30min Oligomycin treatment (grey) in freshly isolated MuSCs from uninjured muscle and 7DPI following CTX. n=2-3 replicates from 1-2 ind. exp. mean ± SD.

(H,I) Oxygen consumption rate (OCR) and Extracellular acidification rate (ECAR) in freshly isolated MuSCs. n=4-6 ind. exp., mean ± SEM.

(J) Immunofluorescence of TA cross-sections at 4DPI. Scale=25µm.

(K) MyoD+ and MyoG+ cells in TA cross-sections at 4DPI. n=6 ind. biol. rep., mean ± SD.

(L-N) Pax7+, MyoD+ and MyoG+ cells in clusters on myofibers cultured for 72hrs. n=3 ind. biol. rep., mean ± SD.
(O,P) Pax7+ (O) and MyoD+ (P) cells in TA cross-sections from the contralateral limb at the indicated times. n=≥3 (O), n=4 (P) ind. biol. rep., mean ± SD.
(Q,R) Pax7+ and MyoG+ cells in clusters on myofibers from 21DPI contralateral limbs following 72hrs in culture. n=3 ind. biol. rep., mean ± SD.
(S) Immunofluorescence of TA cross-sections from contralateral limbs at 4DPI. Red arrows are Pax7+ cells incorporated with EdU, white arrows are Pax7+ cells without EdU incorporation. Scale=50μm.
(T,U) Pax7+ and MyoD+ cells co-expressing EdU or Ki67 in TA cross-sections from contralateral limbs at 4DPI. n=4 ind. biol. rep., mean ± SD.
See also Figure S2

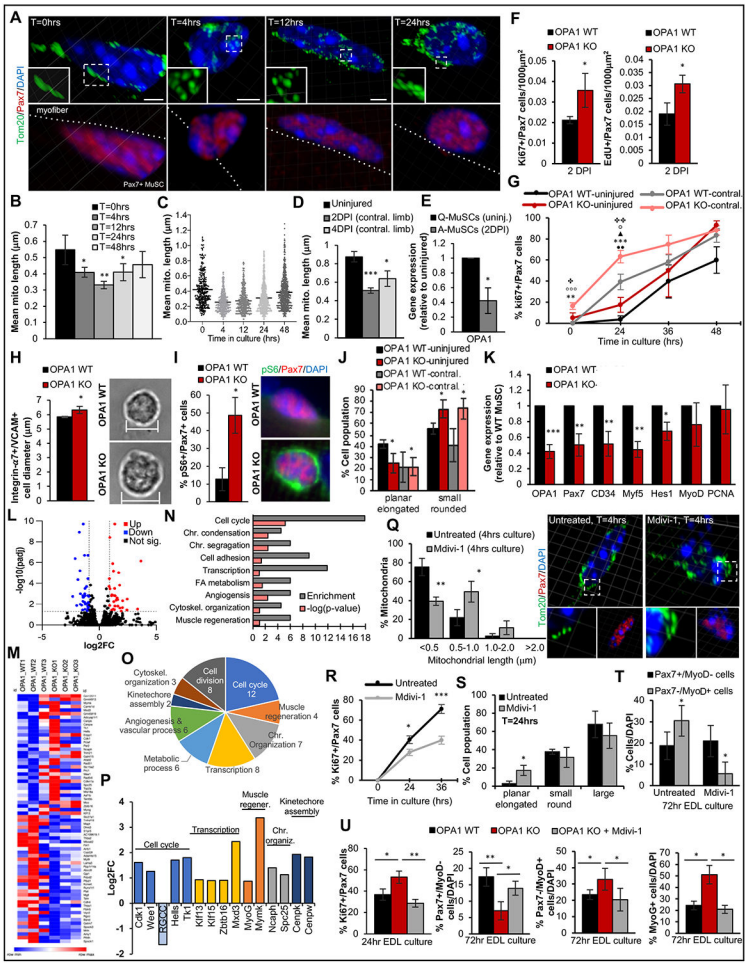

Figure 3. Loss of OPA1 and mitochondrial fragmentation drives the quiescence exit and activation of muscle stem cells.

(A) Confocal 3D reconstruction images of mitochondria (Tom20) in Pax7+ cells during MuSC activation and commitment. Insets are zoomed views of dotted boxes. Scale=2μm.

(B) Mitochondrial length at different time points. n=≥ 100 mitochondria per time point, mean ± SEM.

(C) Distribution plot of mitochondrial length from (B). n=≥100 mitochondria per time point, data are individually plotted and bar is mean.

(D) Mitochondrial length in Pax7+ MuSCs on myofibers from uninjured or contralateral limbs at 2 and 4DPI, n=≥150 mitochondria per condition, mean ± SEM.

(E) qPCR in wild-type MuSCs from uninjured hind-limbs (quiescent-early activation) or injured TAs at 2DPI (activated). n=3 ind. biol. rep., mean ± SD.

(F) Pax7+ cells expressing Ki67 or EdU in TA cross-sections from contralateral limbs at 2DPI. n=3 ind. biol. rep., mean ± SD.

(G) Pax7+ cells expressing Ki67 on myofibers from uninjured or 4DPI contralateral limbs cultured for the indicated times. n=7 ind. exp., mean ± SEM. Statistical symbols indicate the following comparisons; ●WT-Uninjured:WT-contralateral, *WT-uninjured:KO-contralateral, ▲WT-contralateral:KO-uninjured, ○WT-contralateral:KO-contralateral,✤KO-uninjured:KO contralateral.

(H) Cell diameter and transmitted light microscopy images of FACS isolated MuSCs. n=≥ 30 cells per 4 ind. exp., data are mean ± SD.
(I) Quantification and images of Pax7+ MuSCs expressing pS6 on myofibers isolated and fixed immediately. n=3 ind. exp., mean ± SEM.
(J) Pax7+ cells on myofibers with the indicated nuclear morphologies at T=0hrs. Representative images are in Figure S3J. n=7 ind. exp., mean ± SEM.
(K) qPCR in freshly isolated MuSCs. *OPA1* and *Pax7* gene expression levels were also normalized to other housekeeping genes in Figure S3L to confirm results. n=3-6 ind. exp., mean ± SEM.
(L) Volcano plot of differentially expressed genes obtained from RNA-seq. Red and blue dots represent the genes with significantly increased (up) or decreased (down) expression, respectively (padj<0.05).
(M) Heat map of genes significantly up- or down-regulated from RNAseq in MuSCs from OPA1-MKO compared to OPA1-WT. n=3 ind. biol. rep.
(N,O) Gene Ontology (GO) enrichment analysis (N) and pie chart of enriched biological processes (O) from RNA-seq analysis. Values show number of genes significantly altered by padj values.
(P) Log2FC differential gene expression from RNA-seq analysis.
(Q) Confocal 3D projected images of mitochondria (Tom20) and mitochondrial length in MuCSs on myofibers treated with 2μM Mdivi-1 in culture for 4hrs. n=>50 mitochondria per condition, mean ± SEM. Scale=2μm
(R) Pax7+ cells expressing Ki67 on wild-type myofibers cultured for the indicated times without (untreated) or with Mdivi-1. n=5 ind. exp., mean ± SD.
(S) Pax7+ cells on myofibers with the indicated nuclear morphologies following treatment with Mdivi-1 for 24hrs. n=4 ind. exp., mean ± SD.
(T) Pax7+ and MyoD+ cell populations within clusters on wild-type myofibers cultured for 72hrs with or without Mdivi-1. n=5 ind. exp., mean ± SD.
(U) Pax7+ cells expressing Ki67 in myofibers cultured for 24hrs in untreated or Mdivi-1 conditions. n=5 ind. exp., mean ± SEM. Pax7+, MyoD+ and MyoG+ cells in clusters on myofibers cultured for 72hrs untreated or treated with Mdivi-1. n=6 ind. exp., mean ± SD. See also Figure S3

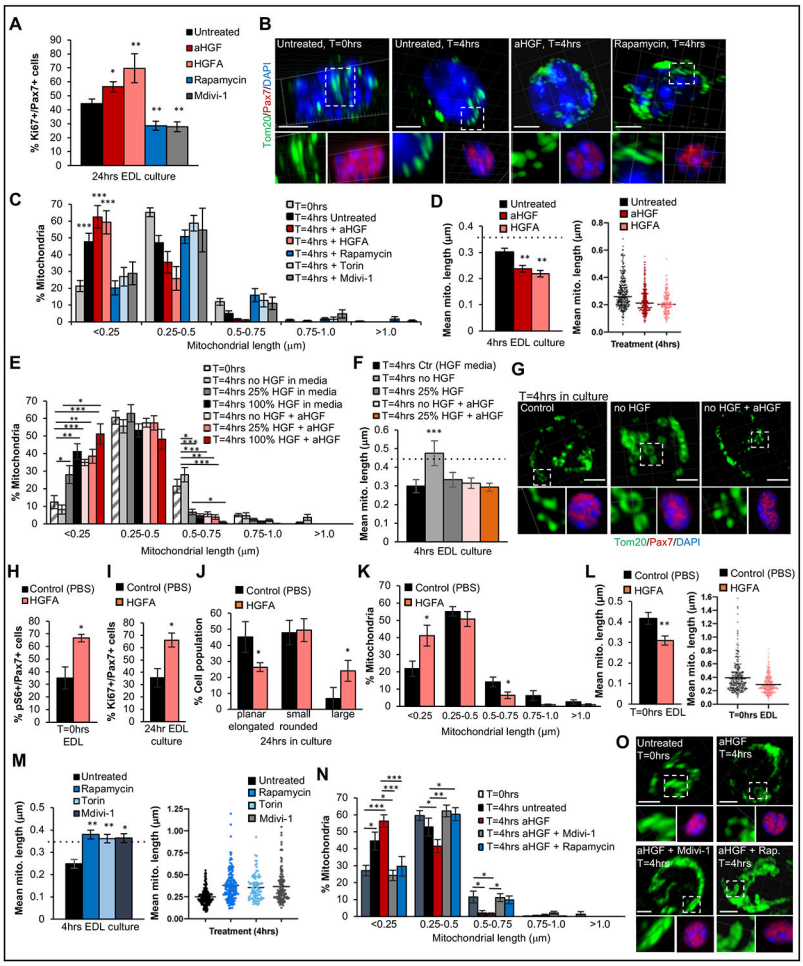

Figure 4. Mitochondrial fragmentation occurs in response to an external activating stimulus to regulate the quiescent state of muscle stem cells.

(A) Pax7+ cells expressing Ki67 on myofibers treated in culture for 24hrs. n=3 ind. exp., mean ± SEM.

(B) Confocal 3D reconstruction images of mitochondria (Tom20) in Pax7+ cells on myofibers treated for 4hrs. T=0hrs is a reference point of mitochondrial shape prior to major changes. Insets represent zoomed views of dotted boxes. Scale=2μm.

(C) Mitochondrial length in Pax7+ MuSCs on myofibers at T=0hrs (no treatment) or after 4hrs in the indicated conditions. n=≥100 mitochondria per condition, mean ± SEM.

(D) Average length and distribution plots from (C). Dotted line is mean mitochondrial length at T=0hrs. n=≥100 mitochondria per condition, mean ± SEM, bar is mean.

(E) Mitochondrial length in Pax7+ MuSCs on myofibers at T=0hrs or cultured for 4hrs with varying HGF concentrations in the medium or supplemented with 10ng/mL recombinant aHGF, n=≥200 mitochondria per condition, mean ± SEM.

(F) Average length from (E). Dotted line is mean mitochondrial length at T=0hrs. n=≥200 mitochondria per condition, mean ± SEM.

(G) Confocal 3D reconstruction images of mitochondria (Tom20) in Pax7+ cells at 4hrs under normal culture conditions (control), HGF deprived media (no HGF), or HGF deprived

media supplemented with 10ng/mL aHGF (no HGF + aHGF). Insets show zoomed view of mitochondria. Scale=2 μm

(H-J) Pax7+ cells expressing pS6 (H), Ki67 (I) or presenting with the indicated nuclear morphology (J) in wild-type myofibers with *in vivo* injection of vehicle control (PBS) or recombinant HGFA and fixed immediately (T=0hrs) after harvest or cultured for 24hrs. n=4 ind. biol. rep., mean ± SEM.

(K) Mitochondrial length binning in Pax7+ cells on wild-type myofibers treated *in vivo* as in (H) and fixed immediately. n=≥50 mitochondria per condition, mean ± SEM.

(L) Mitochondrial length and distribution plot of data from (K). n=>3 ind. exp. with n=≥50 mitochondria per condition, mean ± SEM, bar is mean.

(M) Mitochondrial length and distribution plots from (C) for Rapamycin, Torin and Mdivi-1 treatments. Dotted line is mean mitochondrial length at T=0hrs. n=≥100 mitochondria per condition, mean ± SEM, bar is mean.

(N,O) Mitochondrial length and confocal 3D reconstruction images of mitochondria (Tom20) in Pax7+ cells on wild-type myofibers at T=0hrs or 4hrs. n=≥300 mitochondria per condition, mean ± SEM. Insets represent zoomed views of mitochondria. Scale=2μm. See also Figure S4

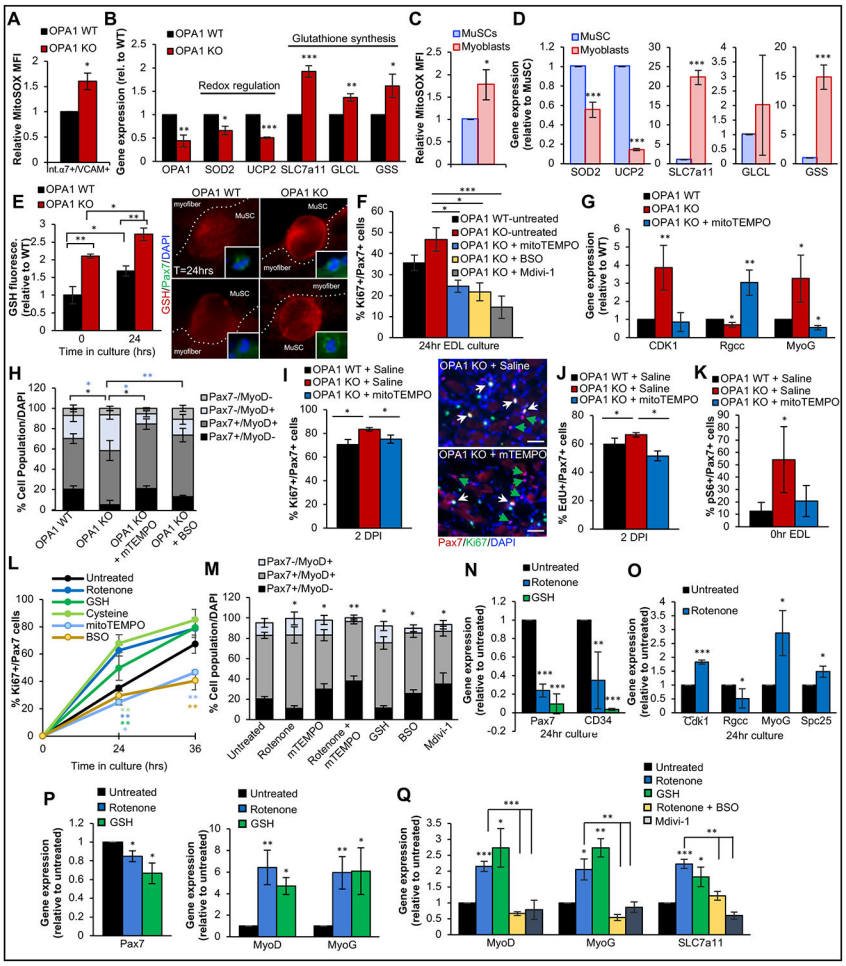

Figure 5. Mitochondrial fragmentation mediates myogenic commitment of muscle stem cells through changes in glutathione and redox states.

(A) MitoSOX mean fluorescence intensity (MFI) using flow cytometry gated on Int.α7+/VCAM+MuSCs. n=4 ind. biol. rep., mean ± SD.

(B) qPCR in freshly isolated MuSCs. n=≥3 ind. biol. rep., mean ± SEM.

(C) MitoSOX MFI by flow cytometry on freshly isolated wild-type MuSCs or primary cultured myoblasts. n=3 ind. biol. rep., mean ± SD.

(D) qPCR in freshly isolated wild-type MuCSs or primary cultured myoblasts. n=≥3 ind. biol. rep., mean ± SEM.

(E) Quantification and representative images of GSH fluorescence in Pax7+ cells on myofibers at T=0hrs and 24hrs. n=4 ind. exp., data are mean ± SD.

(F) Pax7+ cells expressing Ki67 on myofibers treated for 24hrs in culture. n=≥4 ind. exp., mean ± SEM.

(G) qPCR in MuSCs treated for 24hrs. n=3 ind. biol. rep., mean ± SEM.

(H) Pax7+ and MyoD+ cells in clusters on myofibers cultured for 72hrs. n=5 ind. exp., mean ± SEM.

(I,J) Quantifications and representative images of Pax7+ cells co-expressing Ki67 or have incorporated EdU in TA cross-sections at 2DPI from the injured limb of OPA1-WT and

OPA1-MKO mice treated with saline or mitoTEMPO (1mg/kg/day). n=3-4 ind. biol. rep., mean ± SEM.

(K) Pax7+ cells expressing pS6 in myofibers (contralateral limbs) treated as in experiments from (I,J) and fixed immediately (T=0hrs). n=3 ind. exp., mean ± SEM.

(L) Pax7+ cells expressing Ki67 on myofibers at T=0hrs or cultured for the indicated times. n=3 ind. exp., mean ± SEM.

(M) Pax7+ and MyoD+ cells in clusters on wild-type myofibers cultured for 72hrs in the indicated conditions. n=≥3 ind. exp., mean ± SEM.

(N) qPCR in MuSCs treated for 24hrs. n=4 ind. exp., mean ± SD.

(O) qPCR in wild-type MuSCs treated for 24hrs. n=3 ind. exp., mean ± SEM.

(P) qPCR in C2C12 myoblasts treated for 24hrs. Data are normalized to GAPDH. n=≥4 ind. exp., mean ± SEM.

(Q) qPCR in C2C12 myoblasts treated with Rotenone, GSH, Rotenone in the presence of BSO, and Mdivi-1. n=≥3 ind. exp., data are mean ± SEM.

See also Figure S5

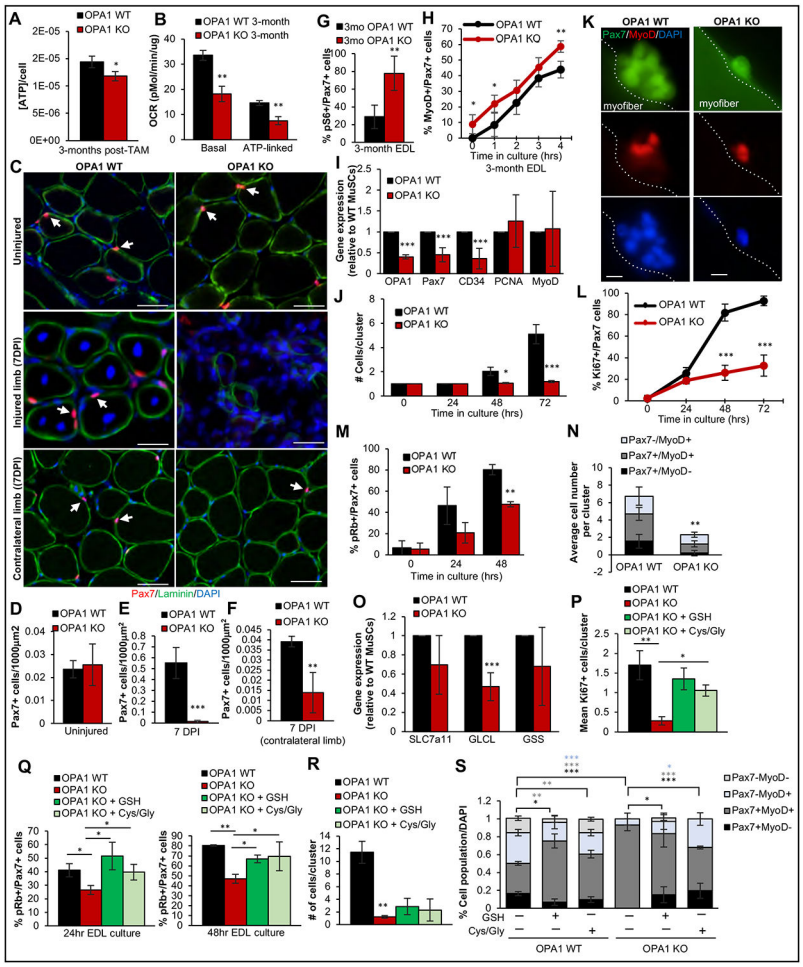

Figure 6. Chronic loss of OPA1 and persistent mitochondrial fragmentation leads to severe muscle stem cell defects.

(A) Total ATP concentration per cell in freshly isolated MuSCs at 3 months post-TAM. n=3 ind. biol. rep., mean ± SD.

(B) Basal and ATP-linked respiration (OCR) in freshly isolated MuSCs at 3 months post-TAM. n=8 OPA1-WT, n=4 OPA1-KO replicates, mean ± SEM.

(C) Immunofluorescence images of TA cross-sections of uninjured limbs or injured and contralateral limbs at 7DPI in 3-month mice. Arrows are Pax7+ cells. Scale=50μm.

(D-F) Pax7+ cells in TA muscle cross-sections of uninjured limbs (D) or injured (E) and contralateral (F) limbs at 7DPI following CTX injection in 3-month mice. n=3 ind. biol. rep., mean ± SD.

(G) Pax7+ cells expressing pS6 on freshly isolated myofibers from 3-month mice. n=3 ind. exp., mean ± SD.

(H) Pax7+ cells expressing MyoD on myofibers from 3-month mice at the indicated times. n=4 ind. exp., mean ± SD.

(I) qPCR in freshly isolated 3-month MuSCs. n=3 ind. biol. rep., mean ± SD.

(J) Cell number within a cluster on myofibers cultured from 0-72hrs. n=6 ind. biol. rep., mean ± SD.

(K) Images of Pax7+ cell clusters on 3-month myofibers cultured for 72hrs. Scale=3μm.

(L,M) Pax7+ cells expressing Ki67 (L) or pRB (M) on 3-month myofibers at T=0hrs or cultured for the indicated times. n=6 (L) n=3 (M) ind. biol. rep., mean ± SD.
(N) Cell population per cluster on 3-month myofibers cultured for 72hrs. n=3 ind. biol. rep., mean ± SEM.
(O) qPCR in freshly isolated 3-month MuSCs. n=3-4 ind. biol. rep., mean ± SD.
(P) Pax7+ cells expressing Ki67 on 3-month myofibers cultured for 72hrs. n=6 ind. exp., mean ± SD.
(Q) Pax7+ cells expressing pRb on 3-month myofibers cultured for 24 and 48hrs. n=3 ind. exp., mean ± SD.
(R) Cells within each cluster on 3-month myofibers cultured for 72hrs. n=6 ind. biol. rep., mean ± SD.
(S) Cell populations on myofibers from the same as in (R). n=6 ind. biol. rep., mean ± SD.
See also Figure S6

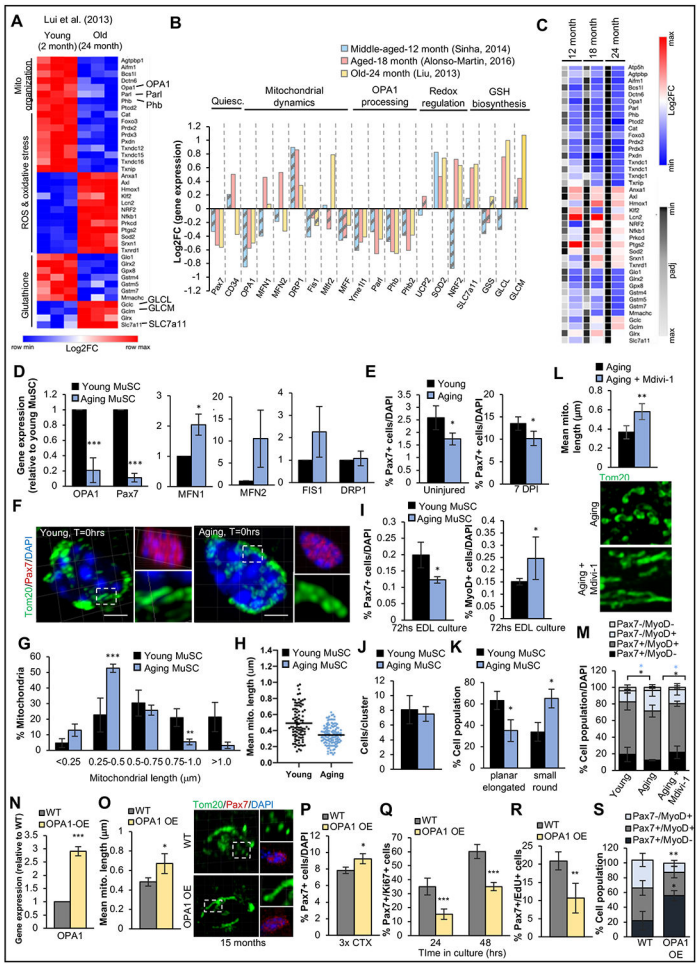

Figure 7. Decreased OPA1 and impaired mitochondrial dynamics are observed during physiological muscle stem cell aging and impact muscle stem cell function.

(A) Heat map of significantly altered genes. n=3 based on a publicly available dataset GSE47177 (Liu et al., 2013).

(B) Log2FC differential gene expression in MuSCs. Dashed bars are non-significant data (padj value <0.05).

(C) Multifactor heat map of altered genes (based on Log2FC). Level of significance is denoted by gradient scale based on padj values, min=high significance.

(D) qPCR in freshly isolated wild-type young (2 month) and aging (12-16 month) MuSCs. n≥3 ind. biol. rep., mean ± SEM.

(E) Pax7+ cells in TA cross-sections from young (2 month) and aging (12-16 month) mice in uninjured conditions or 7DPI following CTX injury. n=3 ind. biol. rep., mean ± SD.

(F) Representative confocal 3D reconstruction images of mitochondria (Tom20) in Pax7+ cells on myofibers from young (2 month) and aging (12-16 month) mice at T=0hrs. Insets are zoomed views of mitochondria. Scale=2μm.

(G,H) Mitochondrial length (G) and distribution plot (H) in Pax7+ cells on myofibers harvested the same as in (F). n=≥100 mitochondria per condition, mean ± SEM.

(I) Pax7+ and MyoD+ cells within clusters on myofibers from young (2 month) and aging (12-16 month) mice cultured for 72hrs. n=3 ind. biol. rep., mean ± SEM.

(J) Cell number in a cluster on myofibers harvested the same as in (I). n=3 ind. biol. rep., mean ± SEM.
(K) Pax7+ cells with the indicated nuclear morphology in myofibers from young (2 months) and aging (12-16 month) mice at T=0hrs. n=3 ind. biol. rep., mean ± SEM.
(L) Length and representative confocal images of mitochondria (Tom20) in Pax7+ cells on myofibers from aging (12-16 month) mice in culture for 72hrs. n=≥100 mitochondria per condition, mean ± SD.
(M) Cell populations on myofibers from young (2 month) and aging (12-16 month) wild-type mice cultured for 72hrs. n=6 ind. biol. rep., mean ± SD.
(N) qPCR in freshly isolated MuSCs from 12-14 months. n=4 ind. biol. rep., mean ± SD.
(O) Mitochondrial length and confocal images of mitochondria (Tom20) in Pax7+ cells on freshly isolated myofibers at 12-14 months. n=3 ind. exp., mean ± SD.
(P) Pax7+ cells in TA cross-sections at 21DPI following third round of CTX injections in aged (15 months) mice. n=4 ind. biol. rep., mean ± SD.
(Q and R) Pax7+ cells co-expressing Ki67 (Q) and EdU (R) on myofibers from aged (12-14 months) mice cultured for 24 (Q,R) and 48hrs (Q). n=4 ind. biol. rep., mean ± SD.
(S) Cell populations in clusters on myofibers from aged (12-14 months) mice cultured for 72hrs. n=4 ind. exp., mean ± SD.
See also Figure S7

Key Resource Table

REAGENT or RESOURCE	SOURCE	IDENTIFIER
Antibodies		
Anti-mouse Pax7	DHSB	Cat# PAX7-S
Anti-rabbit Pax7	Thermo Fisher Scientific	Cat# PA1-117; RRID:AB_2539886
Anti-rabbit Tom20	ProteinTech	Cat# 11802-1-AP; RRID:AB_2207530
Anti-mouse MyoD	Santa Cruz	Cat# sc-32758; RRID:AB_627978
Anti-mouse MyoG	DHSB	Cat# FD5
Anti-rabbit Laminin	Abcam	Cat# ab11575; RRID:AB_298179
Anti-rabbit Ki67	Abcam	Cat# ab15580; RRID:AB_443209
Anti-mouse eMHC	DHSB	Cat# F1.652-s
Anti-rabbit pS6	Cell Signaling Technology	Cat# 4857S
Anti-rabbit pRb	Cell Signaling Technology	Cat# 8516S
Anti-rabbit OPA1	Abcam	Cat# ab42364; RRID:AB_944549
Anti-mouse GAPDH	Abcam	Cat# ab8245; RRID:AB_2107448
Anti-chicken GFP	Abcam	Cat# ab13970; RRID:AB_300798
Anti-mouse Cytochrome C	BD Biosciences	Cat# 556432; RRID:AB_396416
Anti-mouse GSH	Abcam	Cat# ab19534; RRID:AB_880243
Anti-rabbit GSH	Abcam	Cat# ab9443; RRID:AB_307258
Alexa-Fluoro 488 anti rabbit IgG (H+L)	Molecular Probes	Cat# A11008; RRID:AB_143165
Alexa-Fluoro 488 anti mouse IgG (H+L)	Thermo Fisher Scientific	Cat# A11001; RRID:AB_2534069
Alexa-Fluoro 488 anti chicken IgY (IgG) (H+L)	Jackson	Cat# 703-545-155; RRID:AB_2340375
Alexa-Fluor 647 anti rabbit IgG (H+L)	Abcam	Cat# ab150075; RRID:AB_2752244
Alexa-Fluor 647 anti mouse IgG (H+L)	Abcam	Cat# ab150107; RRID:AB_2890037
Alexa-Fluor 594 anti mouse IgG (H+L)	Thermo Fisher Scientific	Cat# A11005; RRID:AB_2534073
Cy3 AffiniPure anti rabbit IgG (H+L)	Jackson	Cat# 711-165-152; RRID:AB_2307443
Cy3 AffiniPure anti mouse IgG (H+L)	Jackson	Cat# 715-165-150; RRID:AB_2340813
Cy3-Conjugated Strepdavidin	Jackson	Cat# 016-160-084; RRID:AB_2337244
Chemicals, peptides, and recombinant proteins		
Biotin	Jackson	Cat# 115-065-205
Mdivi-1	Sigma	Cat# M0199
MitoTEMPO	Sigma	Cat# SML0737
L-Buthionine Sulphoxamine (BSO)	Sigma	Cat# B2515
Rotenone	Sigma	Cat# R8875
mito-Paraquat (mitoPQ)	Abcam	Cat# ab146819
L-Glutathione (GSH)	Sigma	Cat# G4251
L-Cysteine	Sigma	Cat# 5360
Glycine	Bio-Rad	Cat# 1610717
Antimycin A	Sigma	Cat# A8674-50MG
Oligomycin	Sigma	Cat# O4876-25MG
Rapamycin	Invivogen	Cat# tlrl-rap
Torin-1	Invivogen	Cat# inh-tor1

REAGENT or RESOURCE	SOURCE	IDENTIFIER
Recombinant Mouse HGF-A	R&D Systems	Cat# 1200-SE
Recombinant Human HGF (Active form)	Abcam	Cat# Ab632
MitoSOX Red	Thermo Fisher Scientific	Cat# M36008
EdU (5-ethynyl-2'-deoxyuridine)	Baseclick	Cat# BCN-001-500
Critical commercial assays		
CellTiterGlo	Promega	Cat# G9241
TUNEL assay	Roche	Cat# 11684795910
BaseClick EdU detection kit	Sigma	Cat# BCK647-IV-IM-M
PicoPure RNA isolation kit	ThermoFisher	Cat# KIT0214
Rat/Mouse Fibroblast Growth Factor-21 ELISA Kit	Millipore	Cat# EZRMFGF21-26K
Mouse GDF-15 ELISA Kit	Abcam	Cat# Ab216947
Deposited data		
Raw RNA-Seq data	This paper	GEO: GSE208326
Microarray data	(Liu et al., 2013)	GSE47177
Microarray data	(Alonso-Martin et al., 2016)	GSE63860
Microarray data	(Sinha et al., 2014)	GSE50821
RNA-Seq data	(Shcherbina et al., 2020)	GSE121589
Experimental models: Cell lines		
C2C12	ATCC	Cat# CRL-1772; RRID:CVCL_0188
Primary myoblasts	This paper	N/A
Experimental models: Organisms/strains		
Mouse: OPA1-floxed-Pax7CreERT2	This paper	N/A
Mouse: Pax7CreERT2	(Murphy et al., 2011)	RRID:IMSR_JAX:017763
Mouse: Pax7-GFP	(Sambasivan et al., 2009)	N/A
Mouse: OPA1tg (OPA1-OE)	(Varanita et al., 2015)	N/A
Oligonucleotides		
Primers for qPCR, see Table S1	This paper	N/A
Software and algorithms		
FIJI	NIH	https://fiji.sc
Prism GraphPad	GraphPad Software, Inc, 2016	https://www.graphpad.com/
Imaris	Imaris Microscopy Imaging Software	https://imaris.oxinst.com
Flowjo	FlowJo, LLC 2013-2016	https://www.flowjo.com/